FRAGMENTATION ET DÉFORMATION DE LA BANQUISE

MÉMOIRE PRÉSENTÉ

dans le cadre du programme de maîtrise en océanographie

en vue de l'obtention du grade de maître ès sciences

PAR

©JEAN-CHRISTOPHE GAUTHIER MARQUIS

Novembre 2018

Composition du jury :

Louis-Philippe Nadeau, président du jury, Université du Québec à Rimouski

Dany Dumont, Université du Québec à Rimouski

Daniel Bourgault, Université du Québec à Rimouski

Jean-François Lemieux, Environnement et changement climatique Canada

Dépôt initial le 25 avril 2018 Dépôt final le 23 novembre 2018

À Marie-Pier

et Suzie

REMERCIEMENTS

J'aimerais adresser mes remerciements les plus sincères à toutes personnes impliquées de près ou de loin dans ce projet de maîtrise. Merci à mon directeur, Dany Dumont, pour son dévouement et sa passion contagieuse des sciences qui ont grandement contribués à l'épanouissement de ce projet. J'ai beaucoup apprécié nos échanges au cours des dernières années. Ceux-ci m'ont permis de mieux saisir qu'est-ce que de la Science. Merci à mon co-directeur, Daniel Bourgault, pour ses bons conseils tout au long du projet. Dany et Daniel sont tous les deux d'excellents pédagogues qui ont à cœur de donner une formation scientifique de qualité. Merci à Paul Nicot qui a apporté une aide précieuse pour l'acquisition et le traitement des données qui ont rendu possible ce projet. Merci également à Urs Neumeier et son équipe ainsi qu'à Jérémy Baudry pour leur contribution à l'acquisition des données de vagues et de courants. J'aimerais aussi remercier les autres étudiants de ma cohorte ainsi que les enseignants qui ont participé à ma formation. Finalement, merci Marie-Pier pour ton soutien durant ces derniers mois et pour ton sourire ces neuf dernières années.

RÉSUMÉ

La zone de transition entre la banquise et l'océan libre, appelée zone marginale de glace ou *MIZ*, est constituée de morceaux de glace de petite taille appelés floes. Elle est caractérisée par d'importants échanges d'énergie et de quantité de mouvement entre l'océan, la banquise et l'atmosphère, principalement attribuables aux vagues qui fragmentent la glace et qui se propagent sur des dizaines de kilomètres dans la banquise. Les vagues peuvent donc modifier la dynamique de la banquise par l'agitation des floes, l'imposition de forces radiatives et l'amplification des échanges de chaleur. Ces processus jouent potentiellement un rôle majeur dans le climat et la prévision opérationnelle à plus court terme. Ils ne sont toutefois pas représentés dans les modèles numériques actuels, ce qui justifie les nombreux efforts déployés dans les dernières décennies pour mieux les comprendre. Modéliser adéquatement ces phénomènes nécéssite plus d'observations permettant d'étudier les processus en jeu, ce qui constitue l'objectif de ce mémoire. Une caméra autonome installée au sommet du pic Champlain, dans le parc national du Bic situé sur la rive sud de l'estuaire du St-Laurent, est utilisée pour observer et analyser la fragmentation et la déformation de la banquise côtière saisonnière à l'échelle des floes dans le voisinage de la Baie du Ha ! Ha !. La morphologie de la baie, son orientation et sa taille favorisent l'accumulation de glace et sa fragmentation par les vagues générées par les vents d'ouest soufflant sur la polynie de l'estuaire maritime. Le traitement des images prises toutes les deux minutes par la caméra nous permet d'analyser l'évolution spatio-temporelle de trois événements de fragmentation répertoriés durant les hivers 2014 et 2016. L'évolution de la distribution de taille des floes, obtenue par une méthode de segmentation appliquée conjointement avec la vélocimétrie par imagerie de particules *PIV*, montre l'atteinte d'une distribution d'équilibre issue de la fragmentation par les vagues. Un profileur acoustique de courant de type AWAC et des capteurs de pression déployés dans la baie durant l'hiver 2016 permettent de relier les conditions de vagues et les paramètres de la distribution de taille des floes. Une progression saccadée du front de rupture de la banquise est observée pour chacun des événements. La déformation de la banquise obtenue avec la PIV montre clairement l'effet de la fragmentation et permet de relier la déformation à la concentration et la taille des floes.

Mots clés : zone marginale glaciaire, vagues, fragmentation, déformation, photogrammétrie, distribution de taille des floes, banquise

ABSTRACT

The transition zone between pack ice and the ocean, called the marginal zone of ice (MIZ), is composed of small pieces of ice called floes. It is characterized by important exchanges of energy and momentum between the ocean, the pack ice and the atmosphere, mainly due to waves that break up the ice and propagate over tens of kilometers into the ice pack. The waves can thus modify the dynamics of the ice pack by agitating the floes, by imposing radiative forces, and by amplifying heat exchanges. These processes potentially play a major role in the climate and the short-term operational forecast. However, these processes are not represented in the current numerical models, which justifies the many efforts made in recent decades to better understand them. Modeling these phenomena properly requires more observations to study the processes involved, which is the objective of this thesis. A stand-alone camera installed at the summit of pic Champlain in Bic National Park on the south shore of the St. Lawrence Estuary is used to observe and analyze the fragmentation and the deformation of seasonal fast ice at floe-scale in the vicinity of Baie du Ha ! Ha !. Its morphology, orientation and size favors the accumulation of ice and its fragmentation by waves generated by westerly winds blowing on the polynya of the Lower Estuary. The processing of images taken every two minutes by the camera allows us to analyze the spatio-temporal evolution of three fragmentation events captured during the winters of 2014 and 2016. The evolution of the size distribution of the floes, obtained by a method of segmentation applied in conjunction with particle image velocimetry (PIV), shows the achievement of an equilibrium distribution resulting from fragmentation by waves. An acoustic current profiler of the AWAC type and pressure sensors deployed in the bay during the winter of 2016 allow to connect the wave conditions and the parameters of the floe size distribution. A jerky progression of the breaking front of the pack ice is observed for each event. The deformation of the ice pack obtained with the PIV analysis clearly shows the effect of the fragmentation and allows to link the deformation to the concentration and the size of the floes.

Keywords : marginal ice zone, waves, fragmentation, deformation, photogrammetry, floes size distribution, ice pack

TABLE DES MATIÈRES

LISTE DES TABLEAUX

LISTE DES FIGURES

CHAPITRE 1

INTRODUCTION GÉNÉRALE

1.1 Introduction

Au cours des dernières décennies, un important déclin de l'étendue et de l'épaisseur de glace de mer dans l'Arctique a été observé (Comiso, 2012). Ce recul de la banquise, qui s'inscrit dans un contexte de réchauffement climatique, ouvre de nouvelles voies de navigation et facilite l'accès aux ressources naturelles inexploitées de l'Arctique, incluant d'importantes réserves d'hydrocarbures. La diminution de la surface de glace s'accompagne également d'une augmentation de l'énergie des vagues incidentes, celles-ci ayant de plus grands espaces pour se développer (Thomson and Rogers, 2014). La zone marginale de glace, communément appelée MIZ pour *marginal ice zone*, est la zone de transition entre la banquise intérieure et l'océan libre de glace où les vagues de surface influencent significativement l'état de la banquise. En Arctique, cette région peut s'étendre sur des dizaines, voire des centaines de kilomètres depuis la marge de glace. La MIZ est constituée de morceaux de glace en interactions, appelés floes, qui résultent principalement de la fragmentation de la banquise par les vagues. C'est une région généralement moins dense que la banquise, caractérisée par un écoulement beaucoup plus fluide où la taille des floes influence considérablement la dynamique et la thermodynamique (Steele, 1992; Steele et al., 1989). La zone marginale est aussi un endroit où les échanges de quantité de mouvement et de chaleur entre l'océan, la banquise et l'atmosphère sont intenses, notamment en raison de l'action des vagues. En plus de fragmenter la banquise, les vagues agitent et fragmentent les floes, provoquent des collisions, influencent la formation de nouvelles glaces et génèrent de la turbulence (Squire, 2007). Les vagues exercent donc un contrôle dominant sur la dynamique de la MIZ. Pourtant, la MIZ et l'influence des vagues ne sont pratiquement pas représentées dans les modèles opérationnels.

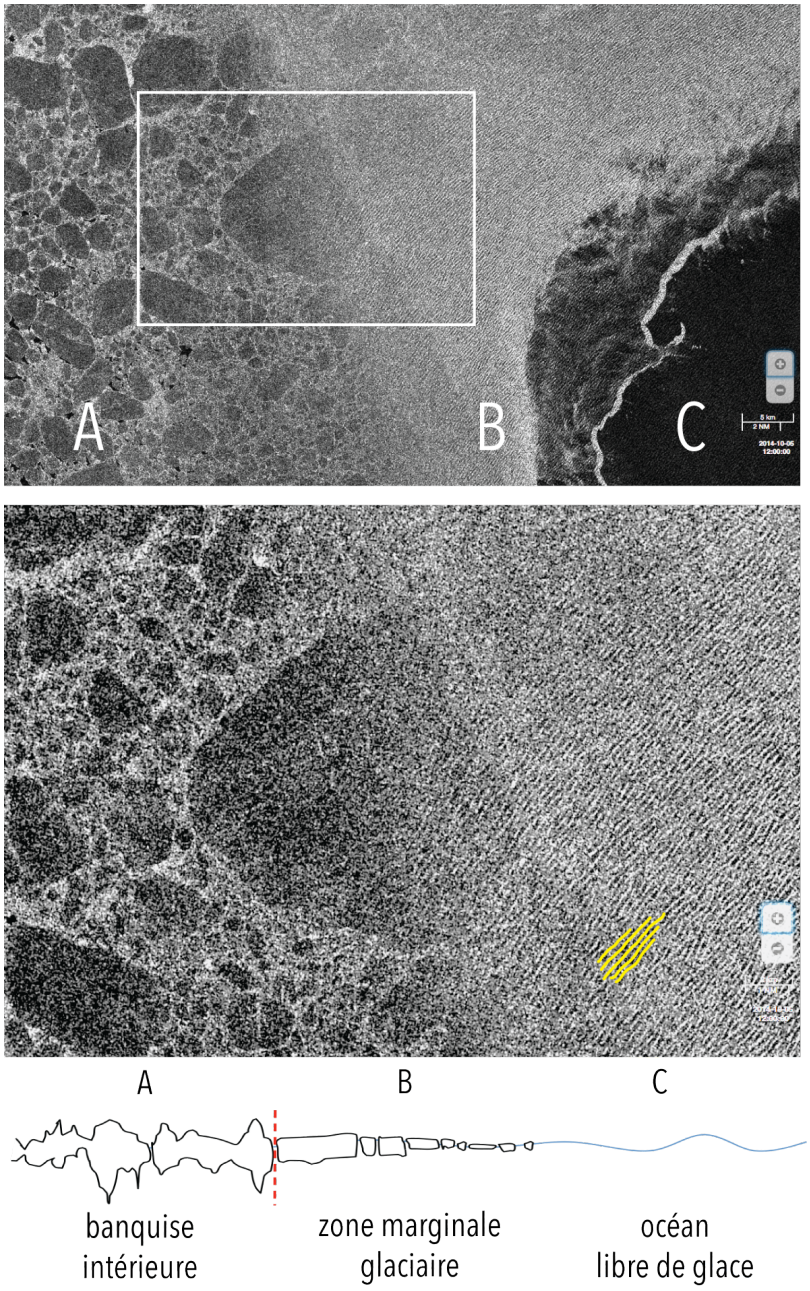

Figure 1: Image radar à synthèse d'ouverture du détroit de Fram (80.8°N, 4.5°O) prise par le satellite Sentinel-1 (Agence spatiale européenne) le 10 octobre 2014 où l'on distingue des vagues générées par le vent dans l'océan libre de glace (C) et se propageant vers le nord-ouest. L'image du bas montre un agrandissement de la zone identifiée par un rectangle où l'on voit des vagues, mises en évidence par les lignes jaunes, d'une longueur d'onde $\lambda \sim 290$ m qui se propagent dans la zone marginale (B) et fracturent un floe d'environ 14 km de diamètre provenant de la banquise intérieure (A). Les floes ne peuvent être distingués dans la zone marginale et la résolution de l'image est de 25 m. Tirée du portail de Ocean Data Lab (https://swarp.oceandatalab.com) dans le cadre du projet SWARP (*Ships and Waves Reaching Polar Regions*).

Générées en eau libre, les vagues peuvent se propager et fléchir le couvert de glace sur des centaines de kilomètres (Squire, 2007; Kohout et al., 2014) (voir Figure 1). Lorsque le fléchissement d'une plaque de glace atteint une amplitude critique, qui dépend de l'épaisseur de la glace, de sa rigidité et de la longueur d'onde des vagues, les contraintes normales aux extrémités verticales, c'est-à-dire à l'interface eau-glace et air-glace, deviennent trop grandes et la banquise se fracture (Langhorne et al., 1998). En supposant que la propagation de vagues est sinusoïdale et monochromatique, la distance entre deux maxima de contrainte est parfois approximée à $\lambda/2$ (Dumont et al., 2011). Cette approximation suppose que la plaque de glace se déforme suivant exactement le profil des vagues incidentes. Toutefois, lorsque des vagues incidentes rencontrent une plaque de glace beaucoup plus longue que la longueur d'onde des vagues, elles se propagent comme des ondes de flexion-gravité de longueur d'onde généralement plus grande que celle de l'onde incidente en eau libre. Mellor (1983) a calculé la distance x_* pour laquelle la déformation d'une plaque semi-infinie est maximale lorsqu'une pression statique est appliquée à son extémité. Il a obtenu la relation suivante

$$x_* = \frac{\pi}{2}\left(\frac{Eh^3}{48\rho g(1-\nu^2)}\right)^{\frac{1}{4}} \tag{1.1}$$

où ρ est la densité de la glace, E le module de Young, g est l'accélération gravitationnelle, h est l'épaisseur de la glace et ν le coefficient de Poisson. Cette équation diffère d'un facteur 2 de celle présentée dans Mellor (1983), dû à une erreur dans la dérivation de l'équation (voir Annexe I). x_*, bien qu'obtenue dans un contexte où la déformation n'est pas causée par les vagues, peut être interprétée comme la taille minimale résultant d'une rupture par flexion de la plaque de glace. Les floes résultant de ces processus de fragmentation forment la MIZ. Toutefois, selon Langhorne et al. (1998), des sollicitations cycliques du couvert de glace par les vagues peuvent diminuer sa résistance à la flexion par effet de fatigue. Dans ce cas, les conditions environnementales passées qui agissent sur la glace devraient être considérées afin de pouvoir correctement prédire la limite de rupture.

La distribution de taille des floes dans la zone marginale de glace (ou FSD pour *floe*

size distribution), ainsi que son évolution dans le temps, dépendent des conditions de vagues. En retour, la FSD modifie la réponse de la zone marginale aux forçages mécaniques (vagues, vents et courants) et thermodynamiques. En effet, d'un point de vue dynamique, la FSD détermine comment le spectre énergétique des vagues est absorbé, diffusé et filtré par la glace. Le modèle de Perrie and Hu (1996) suggère que l'atténuation des vagues dépend principalement de la taille des floes, des conditions de vagues, de la concentration de glace (c'est-à-dire la surface couverte de glace de mer par rapport à la surface libre de glace) et de l'âge des vagues. La taille d'un floe d affecte directement son coefficient de traînée (Steele et al., 1989; Perrie and Hu, 1997). Suivant la notation de Steele et al. (1989), le coefficient de traînée de forme est inversement proportionnel au diamètre du floe ($\tau_{\text{forme}} \propto d^{-1}$), alors que les coefficients de frottement de surface avec l'eau et l'air dépendent de la superficie du floe ($\tau_{\text{surface}} \propto d^{2}$). Les grands floes ont donc tendance à se déplacer plus rapidement que les plus petits lorsque ceux-ci peuvent dériver librement. La taille des floes est donc un paramètre fondamental pour bien comprendre la dynamique de la MIZ.

Les processus thermodynamiques sont aussi affectés par la taille des floes (Steele, 1992). La fragmentation de la banquise tend à augmenter en proportion la surface latérale des floes exposée à la fonte par rapport à la base. Elle peut accélérer la fonte en été, mais peut également favoriser la formation de nouvelle glace dans les interstices entre les floes lors de conditions hivernales, causant le rejet de saumure et générant un transport convectif sous le couvert de glace (Smith and Klinck, 2002). Le rôle de la taille des floes dans les processus thermodynamiques a été longtemps négligé, celui-ci étant dominant seulement pour les floes typiquement plus petits que 30 m (Steele, 1992). Les travaux récents de Horvat et al. (2016) couplant ces processus à des modèles océaniques montrent que bien que l'importance de la taille des floes dans la fonte latérale soit plus grande pour les petits floes, ce processus peut être significatif pour des floes allant jusqu'à 50 km de diamètre. Malgré le fait que plusieurs paramètres n'aient pas été pris en compte dans cette étude, tels que les variations de l'espacement entre les floes et la présence de courant et de turbulence océaniques, ces résultats suggèrent que la taille des floes est un paramètre beaucoup plus important qu'il ne l'était

considéré précédemment dans la modélisation des processus thermodynamiques.

La distribution de taille des floes a été mesurée à plusieurs reprises au cours des dernières décennies, généralement par photographie aérienne ou spatiale. Afin de la modéliser, plusieurs auteurs (Zhang and Skjetne, 2015; Perovich and Jones, 2014; Steer et al., 2008; Toyota et al., 2006; Holt and Martin, 2001; Rothrock and Thorndike, 1984) ont proposé l'utilisation d'une loi de puissance de la forme

$$N(d) = d^{-\alpha} \tag{1.2}$$

où N est le nombre de floes par unité de surface et d est la dimension linéaire des floes. Le paramètre α varie d'une étude à l'autre et sa valeur se situe entre 1.15 et 2.90. Cependant, ces études se concentrent principalement sur les floes de plus de 100 mètres. Toyota et al. (2006) combinent des images obtenues par navire, hélicoptère et satellite afin d'augmenter sa résolution et d'étudier les plus petits floes ($\leq$ 100 m). Leurs analyses suggèrent une distribution à deux régimes composé de deux lois de puissances différentes, l'une pour les floes plus grands que 40 m et l'autre pour les plus petits. L'exposant α est différent pour les petits et les grands floes, ce qui suggère que la FSD n'est pas invariante d'échelle. Le point d'inflexion entre les deux régimes s'expliquerait par des réponses différentes des floes aux forçages mécaniques des vagues selon leur taille. Cette hypothèse est cohérente avec Mellor (1983) qui a calculé que des floes avec des diamètres inférieurs à 40 m sont plus influencés par les processus thermodynamiques que par les forçages mécaniques, leur petite taille les rendant plus résistants à ces derniers. Aussi, Meylan and Squire (1994) ont montré que les déformations verticales diminuent rapidement pour des floes de moins de 100 m, et des résultats obtenus par Perovich and Jones (2014) montrent que sous l'influence de la fonte latérale, la FSD des petits floes dévie d'une loi de puissance, appuyant ainsi l'hypothèse d'un comportement propre aux petits floes. D'autres analyses menées par Toyota et al. (2011) corrèlent avec une distribution à deux régimes (voir Figure 2) et montrent que le point d'inflexion entre les deux régimes est proportionnel à l'épaisseur de la glace, ce qui est cohérent avec la théorie de Mellor (1983)

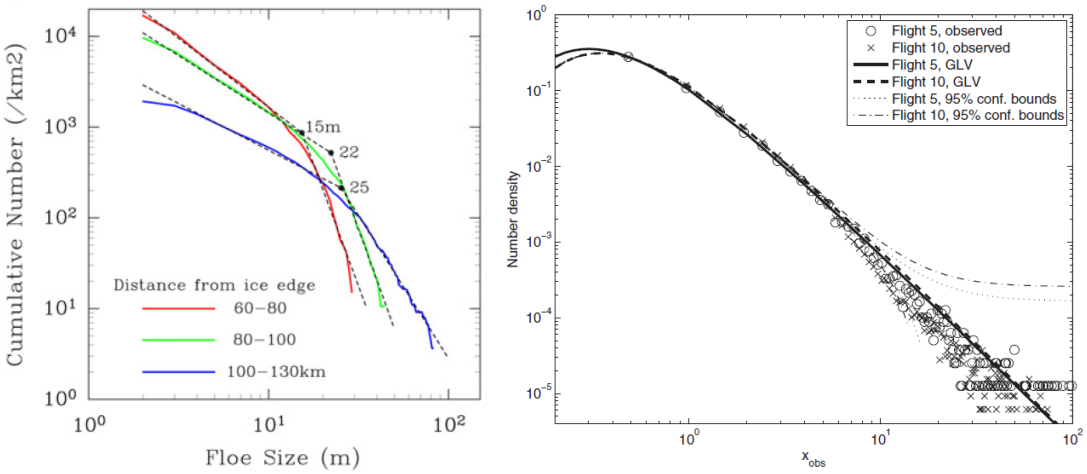

Figure 2: Comparaison entre les interprétations de la FSD par Toyota et al. (2011) (gauche) et Herman (2011) (droite). En utilisant les mêmes observations, Toyota et al. (2011) interprètent la FSD comme une distribution à deux régimes alors que Herman (2011) suggère plutôt une équation généralisée de Lotka-Voltera présentant un maximum.

($x_* \propto h^{3/4}$). La loi de puissance et la distribution à deux régimes sont deux interprétations, mais d'autres auteurs ont proposé un modèle alternatif. Les mêmes observations utilisés par Toyota et al. (2011) ont été corrélées par Herman (2011) avec une équation généralisée de Lotka-Voltera de la forme

$$N(d) = d^{-1-\alpha} e^{(1-\alpha)/d}. \tag{1.3}$$

Ce modèle est une interprétation de la FSD comme un changement graduel dans la distribution qui contraste avec la distribution à deux régimes proposée par Toyota et al. (2011) (Figure 2).

Horvat and Tziperman (2017) présentent un modèle qui inclut à la fois la taille des floes et leur épaisseur via une distribution jointe appelée FSTD pour *floe size and thickness distribution* (Horvat and Tziperman, 2015) et couplé à un modèle de circulation océanique (Petty et al., 2013). Le modèle de Horvat and Tziperman (2017) a l'avantage d'inclure les

effets thermodynamiques mis en évidence par Horvat et al. (2016), la formation de crêtes par compression et le chevauchement (*rafting*) qui sont présents dans la MIZ, mais ignorés des modèles de FSD uniquement. Cela permet de montrer l'émergence de processus différents selon la taille des floes. Selon cette analyse, trois lois de puissance distinctes constitueraient la FSD : une première pour les floes entre 5 et 150 m, dominée par la fragmentation et la perte de glace lors des collisions et de la fusion (ou coagulation) des floes, une seconde pour les floes entre 50 et 150 m principalement marquée par la formation de nouvelle glace et par la fragmentation par les vagues, et finalement, une troisième pour les floes plus grands que 150 m qui dépend directement de la rupture de la banquise, la plupart du temps par les vagues. La classification de ces régimes dépend toutefois des conditions de vagues. Aucun modèle ne fait consensus quant à l'interprétation de la FSD, principalement par manque d'observations reliant les floes (incluant les floes de taille inférieure à 40 m) et les processus physiques qui agissent sur eux. Toutefois, la FSTD représente un élément crucial pour le couplage des modèles de glace et de vagues et la prise en compte des processus couplés.

Un certain nombre de modèles décrivant la déformation de la glace de mer sous l'effet des forçages mécaniques ont été développés au cours des dernières décennies. Les premiers étaient des modèles visqueux (Ruzin, 1959; Reed and Campbell, 1960; Laikhtman, 1958) qui considéèrent la glace comme un fluide newtonien incompressible caractérisé par une relation linéaire entre déformations et contraintes. Des améliorations ont été apportées en introduisant le premier modèle de type élastique-plastique (AIDJEX). Contrairement aux matériaux visqueux, les matériaux plastiques peuvent soutenir des contraintes sans se déformer. Hibler III (1979) a introduit un modèle viscoplastique qui aujourd'hui le modèle le plus largement utilisé pour représenter la dynmaique du couvert de glace. Si la rhéologie viscoplastique fonctionne bien pour des conditions compactes de glace, elle ne décrit par contre pas correctement ce qui se passe dans la zone marginale. Des modèles collisionnels ont été développés afin de prendre en compte les interactions floe-floe. Shen et al. (1986, 1987) ont proposé une rhéologie de collisions visqueuses de la MIZ, mais valable seulement pour la compacité de la glace entre 0.7 et 0.9. Feltham (2005) a proposé un modèle basé sur la théorie des

écoulements granulaires où la rhéologie plastique et visqueuse sont deux cas extrêmes du même modèle. Il utilise le concept de température granulaire, une mesure de l'énergie cinétique d'agitation des floes. Aussi, la taille des floes est un facteur majeur dans la dynamique des modèles collisionnels. Cependant, des lacunes dans notre compréhension des processus dominant l'évolution de la FSD dans la MIZ rendent difficile l'unification de ces deux paramètres dans un seul modèle. De récents progrès pour théoriser un tel processus ont été faits par Dumont et al. (2011) et Williams et al. (2013a,b). Zhang et al. (2015) ont développé un modèle de couplage de taille et d'épaisseur de floes qui décrit l'évolution du FSD dans les MIZ. Les simulations numériques sont cohérentes avec ce modèle, mais à notre connaissance, aucune donnée expérimentale sur l'évolution de la MIZ n'est disponible pour confirmation. Un modèle collisionnel utilisant des floes de tailles et de formes arbitraires a été développé par Rabatel et al. (2015). Il montre qu'à petite échelle (< 10 km^2), le caractère discontinu de la glace dans la MIZ ne peut pas être ignoré pour modéliser sa dynamique. Toutefois, dans l'état actuel, l'action des vagues est absente de ce modèle.

Objectifs

Le présent projet vise à mieux comprendre l'effet des vagues sur la fragmentation et la déformation de la banquise en milieu naturel. Le projet est articulé autour de deux questions :

1. Comment la fragmentation de la banquise par les vagues affecte-t-elle la distribution de taille des floes et leur morphologie ?
2. Quelles sont les caractéristiques de dérive et de déformation de la banquise fragmentée ?

Le caractère original de ce projet repose sur l'étude temporelle des différents processus actifs (fragmentation et déformation) dans la zone marginale de glace. En effet, aucune des méthodes d'échantillonnage citées plus haut ne permet de suivre à l'échelle des floes l'évolution d'un événement de fragmentation de glace par les vagues.

Un objectif implicite mais primordial à la réalisation du projet est le développement d'outils et de méthodes d'analyse afin d'extraire les informations nécessaires pour répondre aux questions 1 et 2. Or, les outils ont été développés dans une optique d'utilisation beaucoup plus large que pour la production des résultats présentés dans ce mémoire. Ils ont été construits pour être réutilisés et modifiés ultérieurement dans divers projets afin de poursuivre les analyses présentées ici.

1.2 Méthodes de traitement d'images

Dans le cadre de ce projet, les principales informations sur les événements de fragmentation de glace sont obtenues par analyse d'images. Plusieurs outils de traitement d'images ont donc été utilisés. Certains de ces algorithmes sont présentés de façon succincte dans la méthodologie à la section 2.2, mais méritent une description plus détaillée. La présente section servira à décrire ces outils de traitement.

Vélocimétrie par imagerie de particules

La vélocimétrie par imagerie de particules (ou PIV pour *particle image velocimetry*) est une méthode initialement développée au début des années 1980 pour étudier la physique des fluides (Adrian, 2005). Cet algorithme permet d'obtenir le champ vectoriel de vitesse de marqueurs contenus dans un fluide. En utilisant un algorithme de corrélation croisée sur une séquence d'images prises à courts intervalles de temps, il est possible de décrire de façon précise le changement de position de groupes de marqueurs (voir Figure 3). Ceux-ci doivent être suffisamment gros pour être visibles sur les images, mais pas trop afin de ne pas perturber l'écoulement du fluide à l'étude, de sorte que leurs déplacements constituent une bonne estimation des mouvements du fluide. Les morceaux de glace de mer peuvent être vus comme de mauvais marqueurs des courants de surfaces, car ils perturbent le transfert de quantité de mouvement, surtout lorsque la concentration de glace est grande. Toutefois, l'algorithme de

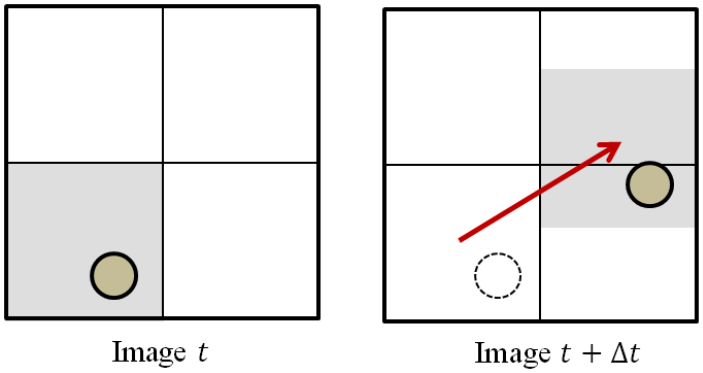

Figure 3: L'algorithme de PIV calcule le déplacement des fenêtres d'interrogations entre deux images en se basant sur le déplacement des traceurs qu'elles contiennent. Dans ce schéma, l'algorithme de PIV tente de déterminer le déplacement de la fenêtre d'interrogation grise. L'algorithme de corrélation croisée consiste à déplacer la fenêtre originale contenant un traceur (cercle foncé) sur la deuxième image et à trouver la meilleur correspondance. Le déplacement final de la zone d'interrogation est représenté par le vecteur rouge. En connaissant le temps entre les deux images, le vecteur de vitesse peut être calculé.

corrélation croisée peut donner une bonne description du mouvement de la glace elle-même.

Dans le cadre de ce projet, la boite à outils Matlab PIVlab 1.41 (Thielicke and Stamhuis, 2014) est utilisée pour calculer le champ de vitesse des floes pendant des événements de rupture de la banquise. L'un des paramètres à considérer lors de l'utilisation de PIVlab est la taille de la zone d'interrogation, qui est définie comme étant la plus petite surface carrée qui sera utilisée par l'algorithme de corrélation croisée afin de calculer le déplacement. Cette zone dicte à l'algorithme la taille de la cellule 2D qu'elle doit suivre d'une image à l'autre, définissant ainsi la résolution du champ vectoriel de vitesse. À la fin du traitement, un test de normalisation médian est appliqué sur le résultat afin de comparer chacun des vecteurs avec ses voisins directs. Si la valeur d'un vecteur est supérieure à sept fois l'écart-type entre ses voisins, le vecteur est considéré comme aberrant. Il est donc supprimé et remplacé par une valeur issue d'une interpolation linéaire. Le lecteur est référé à Thielicke and Stamhuis (2014) pour plus de détails sur l'algorithme PIVlab 1.41.

Algorithmes de segmentation

L'un des défis de l'analyse d'images de glace en zone marginale est d'utiliser un algorithme de traitement qui distingue la glace de l'eau. Plusieurs algorithmes sont présents dans la littérature, mais le plus répandu est la méthode par valeur seuil (*threshold value method*). Cette méthode se base sur un critère de luminosité pour différencier l'eau de la glace (Lytle et al., 1997; Holt and Martin, 2001; Toyota et al., 2006, 2011). La glace possède généralement un albédo supérieur à l'eau de mer. Il est alors possible de choisir une valeur seuil de luminosité qui permet de faire la distinction entre les deux et d'obtenir une image binaire : noir pour les pixels ayant une valeur de luminosité inférieure à la valeur seuil et blanc pour les autres. Lorsque les concentrations de glace sont faibles et les floes assez grands, cette méthode fonctionne bien puisque la majorité des floes ne sont pas en contact les uns avec les autres. Dans le cas contraire, une étape de traitement supplémentaire est nécessaire afin de séparer les floes qui se touchent.

Plusieurs algorithmes différents sont utilisés afin de pallier à ce problème. Certains auteurs (Paget et al., 2001; Steer et al., 2008; Banfield and Raftery, 1992) utilisent la méthode érosion-expansion. L'idée principale de cette méthode est d'appliquer un algorithme d'érosion qui soustrait les pixels sur la frontière extérieure de chaque objet dans l'image, ce qui permet de séparer en plusieurs morceaux les floes anisotropes et de recréer l'image initiale en incluant les séparations artificielles. Un autre algorithme permettant d'isoler les floes en contact est la méthode des bassins versants ou *watershed* (Zhang et al., 2013; Blunt et al., 2012). Cet algorithme traite les images comme des cartes topographiques ayant comme sommets le centre des objets et trace des lignes artificielles entre les sommets adjacents. Cette méthode est celle choisie dans ce projet et est expliquée en détails plus loin.

L'algorithme *snake gradient vector flow* (GVF) utilisé par Zhang and Skjetne (2015) est un bon exemple d'une méthode de traitement plus complexe. Le principe est le suivant. La méthode de valeur seuil est utilisée pour extraire la glace émergée appelée *glace claire*.

Puisque la glace submergée, appelée *glace sombre*, possède un albédo significativement plus faible que la glace immergée, elle est rarement détectée par la méthode de valeur seuil. Un partitionnement en k-moyennes (Macqueen, 1967) est utilisé pour identifier et différencier des regroupements, ou clusters, et ainsi mieux détecter ce type de glace. Ces regroupements se font selon l'intensité *RGB* (*Red Green Blue*) des pixels présents dans l'image. Zhang and Skjetne (2015) partitionnent les pixels en trois groupes ($k = 3$) : la glace claire, la glace sombre et l'eau. La glace claire et la glace sombre sont toutes les deux utilisées par l'algorithme GVF pour une meilleure détection des bords. La glace claire et sombre agissent à titre d'agent répulsif sur des splines libres de se déplacer sur l'image (Xu and Prince, 1998). La glace pousse et déforme la spline sur l'image de sorte qu'elle épouse la forme des floes, ce qui facilite la détection de bordures.

Malgré les progrès importants dans les algorithmes de détection d'objets, aucune méthode de traitement totalement automatique n'existe et ce champ de recherche est encore en plein développement. Dans le présent travail, une méthode par valeur seuil combinée à une méthode des bassins versants sont utilisées. Voici le détail de l'algorithme utilisé dans le cadre de ce projet.

Afin de séparer la glace de l'eau, la méthode à valeur seuil a été appliquée sur les images. Les valeurs *RGB*, des valeurs entières entre 0 et 255, sont moyennées pour obtenir une intensité $I = (R+G+B)/3$ donnant une image en niveaux de gris (Figure 4a). Le contraste entre l'eau et la glace est ensuite ajusté (Figure 4b) et une valeur seuil d'intensité $I_c(n)$ est choisie manuellement entre l'intensité de la glace $I_i(n)$ et celle de l'eau $I_w(n)$ pour chaque image n. Cette méthode à valeur seuil est utilisée pour créer une image binaire qui sera utile pour l'analyse ultérieure des floes, où $\tilde{I}(I \geqslant I_c) = 1$ et $\tilde{I}(I < I_c) = 0$. Puisque l'intensité lumineuse extérieure varie avec l'heure et les conditions météorologiques, une seule valeur seuil ne peut être utilisée pour toutes les images et tous les événements. Cette étape nécessite donc une optimisation manuelle, par essais et erreurs. Même dans des conditions idéales, la séparation par valeur seuil ne peut segmenter les floes en contact. C'est pourquoi une étape

additionnelle est nécessaire. Dans le cadre de ce projet, un algorithme basé sur la méthode des bassins versants a été choisi.

Lorsque deux floes sont en contact, le résultat sur l'image binaire est un seul floe ayant une forme géométrique biscornue et possédant généralement des concavités. Dans ce cas, le ratio entre le périmètre au carré P^2 et l'aire A est plus grand que pour un floe typique de forme plus circulaire. Le ratio isopérimétrique défini par

$$\Gamma \equiv \frac{P^2}{4\pi A} \tag{1.4}$$

indique combien la forme est différente d'un cercle. Pour un cercle parfait, la valeur de Γ est 1 alors que pour un rectangle quatre fois plus long que large, par exemple, $\Gamma = 25$. Une forme binaire ayant un ratio isopérimétrique plus grand qu'une valeur critique Γ_c choisie manuellement est considérée comme étant composée de deux ou plusieurs floes en contact, ou un floe ayant une forme instable qui est sur le point de se rompre. Pour ces formes, un algorithme de bassins versants est utilisé pour trouver le ou les points de contact entre les floes (localisation des points faibles de la forme) où la forme doit être artificiellement brisée.

La méthode des bassins versants traite les formes binaires comme des surfaces topographiques. Pour ce faire, chaque pixel blanc (glace) se voit associer la distance euclidienne minimale avec le pixel noir (eau) le plus proche. Les floes sont ainsi transformés en champs de distance et leurs centres correspondent à des maxima locaux. Lorsque plusieurs floes sont en contact, leurs maxima seront séparés par des vallées, c'est-à-dire une suite de minima locaux. Une valeur seuil, déterminée manuellement par essais et erreurs afin d'éviter la sous-segmentation et la sur-segmentation, servira à tracer une ligne noire sur l'image binaire reliant les minima locaux. Cette ligne est appelée *ligne de crête de bassins versants*. Afin de prévenir la sur-segmentation, qui est très fréquente avec cette méthode, une intensité minimum $I_i(n)$ pour laquelle les pixels de glace ne peuvent pas être modifiés par l'algorithme des bassins versants est choisie, de sorte que $256 \geq I_i(n) \geq I_c(n)$. Dans ce projet, $I_i(n)$ a été défini comme étant $I_c(n) + 30$. Aussi, pour plusieurs des analyses qui vont suivre, les valeurs obtenues de

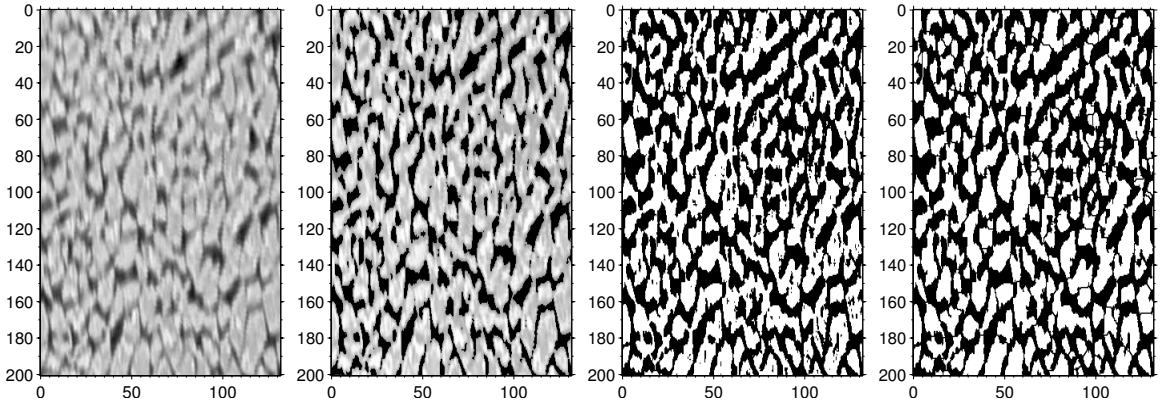

(a) Intensité RGB (b) Contraste ajusté (c) Image binaire (d) Segmentation et remplissage

Figure 4: Quatre étapes du processus de traitement d'image : a) les valeurs *RGB* sont moyennées et une image en niveaux de gris est construite ; b) le contraste de l'image est ajusté ; c) l'image binaire est obtenue de la méthode à valeur seuil ; et d) le résultat final est obtenu après l'application de la fragmentation par méthode des bassins versants. Les dimensions sont en mètres.

trois images séparées de deux minutes chacune sont prises et moyennées afin de minimiser l'erreur aléatoire associée au traitement d'images. Par exemple, deux floes en contact qui seraient comptés comme un seul floe sur une seule image pourraient être séparés sur l'image subséquente, minimisant ainsi l'erreur. À la fin du processus, chacun des floes est numéroté et les informations à propos de l'aire, du périmètre et de l'excentricité sont calculées. Les floes composés de moins de six pixels sont retirés de l'analyse puisqu'ils sont susceptibles d'être des erreurs de détection (reflets à la surface de l'eau, glace submergée, impureté sur l'image, etc.). Les floes sont considérés comme pleins, c'est-à-dire qu'aucun pixel d'eau n'est permis à l'intérieur des frontières d'un floe. À la fin de l'analyse, les floes sont donc remplis artificiellement afin d'enlever les trous associés à des imperfections de l'image. L'ensemble du processus est présenté à la Figure 4 et, afin de montrer plus en détails le travail fait par l'algorithme des bassins versants, un zoom sur quelques floes est présenté à la Figure 5.

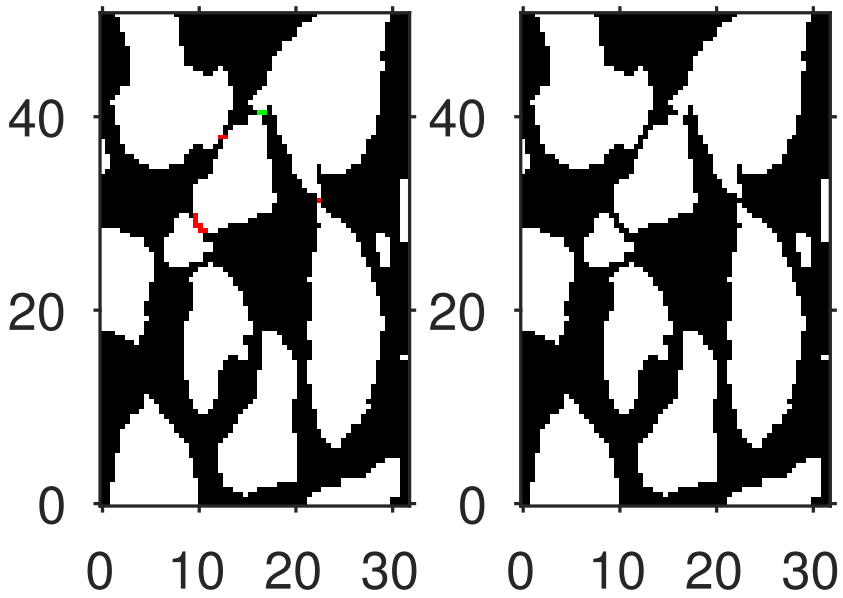

(a) Avant le traitement (b) Après le traitement

Figure 5: Exemple de traitement avec l'algorithme des bassins versants. La figure de gauche représente une image binaire obtenue avec la méthode à valeur seuil. Sur celle de droite, les pixels rouges sont ceux supprimés par l'algorithme des bassins versants et les pixels verts sont ceux qui ne le sont pas, mais qui auraient dû l'être. Il y a sous-segmentation (pixels verts), ce qui implique que ces deux floes compteront pour un seul. Les dimensions sont en mètres.

Transformée de Fourier

La longueur d'onde des vagues λ est obtenue de trois manières différentes décrites à la section 2.2. Sans appareil de mesure *in situ*, cette information peut être obtenue à partir des images en mesurant la distance en pixels entre les crêtes. Toutefois, afin d'éviter le plus possible le nombre de mesures faites directement sur les images, la transformée de Fourier discrète en deux dimensions a été utilisée. Avec cette méthode, il est possible de connaître le spectre de vagues ainsi que sa direction. En effet, la transformée de Fourier 2D, lorsqu'elle est appliquée sur une portion de l'image où un champ de vagues est bien visible (voir Figure 6), analyse les périodicités présentes dans l'image et produit un spectre 2D composé de fréquences spatiales dont l'amplitude est représentée en tons de gris. L'intensité des pixels est proportionnelle à l'amplitude de présence de certaines fréquences (voir Figure. 7). Plus les pixels sont près du centre, plus il s'agit de basses fréquences. Les spectres spatiaux d'images de vagues sont généralement composés d'un nuage de points au centre (ces basses fréquences sont toujours présentes car il ne suffit que de deux pixels éloignés sur l'image de départ pour que la transformée de Fourier voit une périodicité) et de deux nuages de points, symétriques par rapport au centre, qui correspondent au spectre des vagues. Ces nuages de points correspondent aux fréquences positives et négatives de la transformée de Fourier rapide, ce qui explique pourquoi elles sont symétriques par rapport au centre. En pratique, il est parfois difficile de distinguer dans le spectre les nuages de points associés aux vagues. Les principaux facteurs rendant l'application de cette méthode difficile en milieu naturel sont la présence d'objets dans l'image (glace, côte, floes et autres), la clareté de l'image, les reflets à la surface de l'eau ainsi que les effets de bord souvent présents lorsque l'on applique la transformée de Fourier à une image.

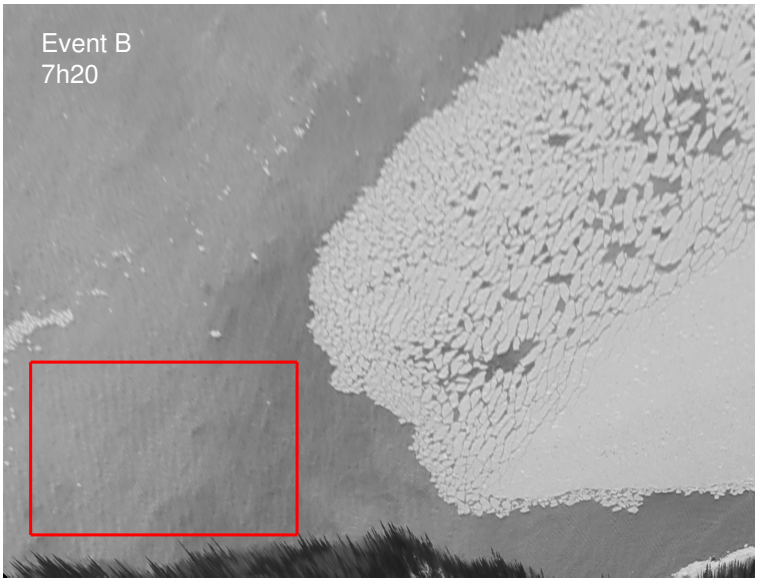

Figure 6: La zone délimitée par le carré rouge est une région propice à l'application de la transformée de Fourier, car les vagues y sont clairement visibles et aucun objet flottant n'est présent. Le spectre spatial de cette zone est présenté à la Figure 7.

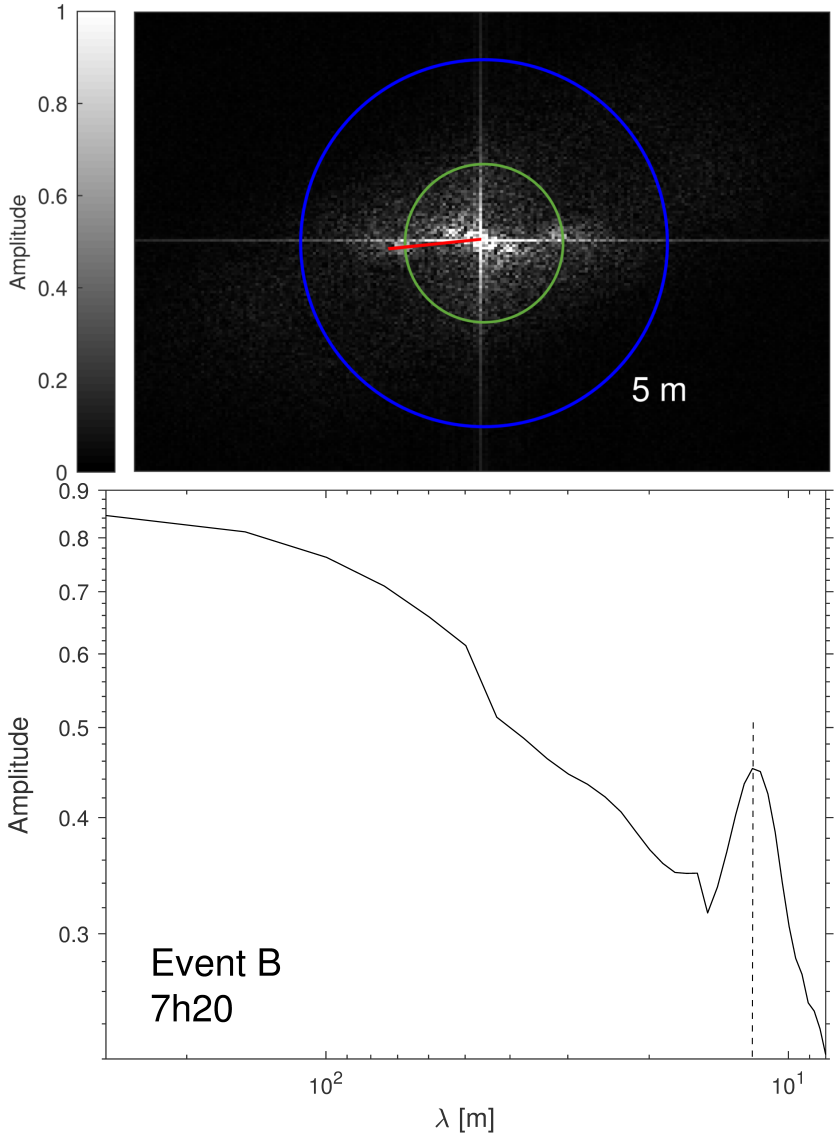

Figure 7: **Haut** : Un zoom au centre du résultat de la transformée de Fourier du carré rouge de la Figure 6 est présenté. On peut y voir deux pics distincts correspondant à la houle provenant de l'ONO ($\lambda \sim 25 \pm 2$ m) et les vagues plus courtes de l'OSO ($\lambda \sim 12 \pm 2$ m). Le contour bleu correspond à une longueur d'onde de 5 m. **Bas** : Un transect passant par le centre du spectre spatial et l'un des pics correspondant aux vagues plus courtes est présenté. Ce transect correspond à la ligne rouge sur la figure du haut. Une ligne pointillée montre la longueur d'onde centrale qui est de 12 m. Un filtre gaussien a d'abord été appliqué sur le spectre spatial afin de le lisser.

CHAPITRE 2

TIME-RESOLVED OBSERVATION OF WAVE-INDUCED ICE BREAK-UP EVENTS

2.1 Introduction

The transition region between the ice pack and open sea, usually called the marginal ice zone or *MIZ*, is an area where the dynamical processes are highly influenced by waves. In the Arctic, this region can extend for tens or even hundreds of kilometers from the ice edge. This region consists of pieces of ice, called floes, which result mainly from the fragmentation of the pack ice by the waves. Those waves, generated by wind in open water, can propagate hundreds of kilometers into the ice cover inducing flexural strain in the material (Squire, 2007; Kohout et al., 2014).

According to the Euler-Bernoulli theory (Kerr and Palmer, 1972), the relation between the normal stress σ_x at the vertical ends of a semi-infinite ice plate and the strain ε_x in given by

$$\sigma_x = E\varepsilon_x = E\frac{h}{2}\frac{\partial^2\eta}{\partial x^2} \tag{2.1}$$

where x is the x-axis aligned with the wave propagation direction, η is the deflection generated by the waves, h is the thickness of the ice plate and E is the Young modulus. When the deformation generate stresses higher than the flexural strength, the ice plate breaks up. The floes that result from this process constitute the MIZ. Assuming the propagation of sinusoidal waves, the distance between two stress maxima is sometimes approximated to $\lambda/2$ (Dumont et al., 2011). This distance can be seen as an order of magnitude for the size of the floes that will separate from the pack ice. However, when incident waves encounter a plate of ice

that is much longer than the wavelength of the waves ($L \gg \lambda$), they propagate as bending-gravity waves of wavelength generally longer than the incident wave in open water. Since the plate has zero deformation at its free end, it could be assumed that the fracture caused by the bending of the plate occurs at a certain distance depending on the properties of the pack ice. Mellor (1983) calculated the distance x_* at which the deformation of a semi-infinite plate is maximal when pressure is applied at its end. He obtained the following equation

$$x_* = \frac{\pi}{2}\left(\frac{Eh^3}{48\rho g(1-\nu^2)}\right)^{\frac{1}{4}} \tag{2.2}$$

where ρ is the density of the ice, g the gravitational acceleration and ν is the Poisson's ratio. It should be noted that this equation differs from that of Mellor (1983) by a factor of 2 due to an error in Mellor's derivation (see Annexe I for the derivation). This value, although obtained from a situation where the deformation is not caused by a wave but by a static pressure, is interpreted as being the minimum size of a floe resulting from a bending fracture. However, according to Langhorne et al. (1998), cyclic wave loading by the waves can decrease its flexural strength through fatigue processes. In this case, past environmental conditions that acted on the ice should be considered in order to predict the breaking stress.

The floe size distribution, or *FSD*, and its evolution in the MIZ are largely affected by the wave condition. In return, the FSD changes the response of the MIZ to thermal and mechanical forcing. In fact, the floe size is an important parameter for both dynamical (wind, wave and current) and thermodynamical processes. First, from a dynamical point of view, the FSD determines how the wave energy spectrum is absorbed, scattered and filtered by the ice (Squire and Moore, 1980). Perrie and Hu (1996) have shown that the wave attenuation factor of the MIZ depends mostly on the floe size, wave conditions, the ice concentration (fraction of ice-covered area) and wave age. Secondly, the size of a floe (along with the ice concentration and draft) directly affect its form drag stress τ_{form} (Steele et al., 1989; Perrie and Hu, 1997). The form drag is inversely proportional to the diameter of the floe ($\tau_{form} \propto d^{-1}$). The air-ice skin drag and the water-ice skin drag also depend on the size of the floes. Thus, the air-ice-

ocean momentum exchange in the MIZ partially depends on the FSD. Thirdly, the breaking of the ice plate into a collection of floes also has an impact on thermodynamical processes (Steele, 1992). An increase of lateral surfaces exposed to water can accelerate the melting of the ice. But the same process can help the formation of new ice in the openings between floes under winter conditions. This phenomenon can cause brine rejection during freezing leading to convective transport under the ice cover (Smith and Klinck, 2002). The floes size importance in the thermodynamical processes is sometimes overlooked following the hypothesis that since the ratio of lateral surface on total surface of big floes (30 m and more) is very small, those floes are not significantly affected by lateral melt. However, experiments done by Horvat et al. (2016) on ocean models show that although the size of the floes in lateral melt is more important for small floes, this parameter remains significant for floes up to 50 km. Despite the fact that several parameters were not taken into account in this study (such as the change of space between floes and the presence of current and ocean turbulence), these results suggest that floe size is more important for thermodynamic processes than previously considered.

The FSD has been measured in the MIZ many times over the years through aerial and spatial photography. The challenge is to isolate the individual floes on the images, which are touching each other in crowded ice floe images. The threshold value method, which uses a luminosity criterion, is widely used to distinguish the ice from the water (Lytle et al., 1997; Holt and Martin, 2001; Toyota et al., 2006, 2011). It works well when the concentration of ice on a picture is low (i.e. almost all floes are separated from each other), but floes in contact are not separated by this method and thus count as one big floe. Some authors use the erosion-expansion method to overcome this issue (Paget et al., 2001; Steer et al., 2008; Banfield and Raftery, 1992). Others use a watershed method (Zhang et al., 2013; Blunt et al., 2012). The snake gradient vector flow (GVF) algorithm used by Zhang and Skjetne (2015) is a good example of a more complex processing method that combines threshold value method, *k-means* partitioning (Macqueen, 1967) and snakes algorithm (Xu and Prince, 1998) for a better edge detection. Despite significant progress in object detection algorithms, no fully

automatic processing method exists and this research field is still in full development. In this work, the threshold value method and the watershed method are used.

In a attempt to synthesize FSD results, many authors (Zhang and Skjetne, 2015; Perovich and Jones, 2014; Steer et al., 2008; Toyota et al., 2006; Holt and Martin, 2001; Rothrock and Thorndike, 1984) have proposed to describe it with the following power law

$$N(d) = d^{-\alpha} \tag{2.3}$$

where N is the number of floes per unit area with diameter smaller than d. Those studies were mainly focused on large floes (larger than 100 m) and the value of α varies from studies between 1.15 and 2.90. Toyota et al. (2006) combined ship-borne, helicopter-borne, and Landsat images in order to increase the resolution of the smallest detectable floes (below 100 m) and suggested a two-regime distribution, i.e. two different power laws in the same distribution. One for floes larger than 40 m and another one for smaller floes with α being less than 2, suggesting that different processes act on small floes and the FSD is not scale invariant. This is coherent with Mellor (1986) who calculated that floes with less than 40 m diameter are more driven by thermodynamical processes since they are more resistant to mechanical forcing. Results from Perovich and Jones (2014) show that under the influence of lateral melting, the FSD deviates from a power law for small floes, which is consistent with Mellor (1986) and Toyota et al. (2006). Further analysis correlates with the two-regime distribution and show a correlation between ice thickness and the point of inflection between the two regimes (Toyota et al., 2011). The two-regime distribution is one interpretation of the data and other authors have proposed alternate models to the two-regime postulate. Herman (2011) proposed a generalized Lotka-Volterra equation to fit observed FSD:

$$N(d) = d^{-1-\alpha} e^{(1-\alpha)/d} \tag{2.4}$$

This model interprets the FSD as a gradual change in the distribution which contrasts with

the the previous interpretation. No single model is widely accepted because of the lack of observations linking the size of the floes (including floes under 40 m) to the physical processes acting on them. Horvat and Tziperman (2017) presents a model that includes both floe size and thickness (the FSTD for *floe size and thickness distribution* described by Horvat and Tziperman (2015)), coupled with an ocean circulation model (Petty et al., 2013). The model has the advantage of including the thermodynamic effects highlighted in Horvat et al. (2016) (see above), the rafting and ridging that are present in the MIZ, but ignored in FSD models. This allows to show the emergence of different processes depending on the size of the floes. According to this analysis, three distinct power laws would constitute the FSD: one for floes between 5 and 150 m dominated by fragmentation and loss of ice during collisions and the merging of floes, a second for floes between 50 and 150 m dominated by the formation of new ice and fragmentation by waves, and finally, a third for floes larger than 150 m which depends directly on the breaking of the pack ice, most of time by the waves. The classification, however, depends on wave conditions. There is no consensus on the interpretation of FSD, mainly due to a lack of observations linking floes (including floes smaller than 40 m) and the physical processes that affect them, but FSTD is a crucial element for the coupling of ice and wave models and the consideration of coupled processes.

A number of sea ice dynamic models have been developed for the pack ice over the last few decades. The first ones were viscous models (Ruzin, 1959; Laikhtman, 1958; Reed and Campbell, 1960), which consider ice as an incompressible Newtonian fluid with a linear relation between deformation and stress. Improvements have been made by introducing the first plastic model (AIDJEX). Unlike viscous material, plastics can account for non-reversible phenomena such as ice ridging. Hibler III (1979) derived a viscous-plastic model that have been considered as the reference model for ice cover. Collisional models were developed in order to account for interacting floes in the MIZ. Shen et al. (1986) proposed a collisional rheology resulting in a viscous, non-plastic view of the MIZ but only valid for ice compactness between 0.7 and 0.9. Feltham (2005) proposed a model based on granular flow theory where plastic and viscous rheology are two extreme cases of the same model. Those behav-

iors depend on the *granular temperature*, a measure of kinetic energy of flow fluctuation, and ice concentration. Floe size is a major factor in collisional models dynamics. However, gaps in our understanding of the FSD and MIZ processes make it difficult to unify both into a single model. Recent progress have been made to theorize such processes by Dumont et al. (2011) and Williams et al. (2013a,b). One particular problem is the evolution of the FSD in the MIZ, which is needed in order to include the MIZ in larger scale models. Zhang et al. (2015) developed a model coupling floes size and thickness that describe the evolution of the FSD in the MIZ. The numerical experiments of Zhang et al. (2015) are coherent with the FSD theory but, to our knowledge, no experimental data of evolution of the MIZ are available for confirmation. A collisional model using floes of arbitrary sizes and shapes was developed by Rabatel et al. (2015). It shows that on a small scale (< 10 km ^{2}), the discontinuous nature of the ice in the MIZ can not be ignored in models. However action of the waves is currently absent from this model.

In this paper, a low-cost photogrammetric method is used to capture wave-induced break-up events in the St. Lawrence Estuary, Canada, which provides new informations about the spatio-temporal evolution of the sea ice at high resolution (few meters) in relation with wave conditions. Waves are assumed to be the main factor of fragmentation. Informations about floe morphology is extracted using semi-automatic image processing algorithms, including a watershed segmentation and a particle image velocimetry (PIV) algorithm. Section 2.2 describes the study site, the experimental setup, and the image processing algorithms used to extract results, which are presented in section 2.3. Results are discussed in section 2.4.

2.2 Methodology

2.2.1 Study site and experimental setup

The St. Lawrence Estuary is the largest in the world. It is covered with ice in winter and connects the St-Lawrence river, which drains a 1.6 millions km^2 pool, to the gulf and North-

West Atlantic. It is the southernmost place in the northern hemisphere where an extensive sea ice cover still forms during winter. The study site is located on the south shore of the St. Lawrence Estuary, specifically in Baie du Ha! Ha! in the Bic National Park (see Figure 8). Sea ice is generally present in the estuary from December to April (Galbraith et al., 2014). The study of wave-ice interactions is suitable to this area particularly because of the presence of a polynya in the west, between Rimouski and the head of the Laurentian Channel, near the mouth of the Saguenay River (Figure 9). This polynya allows wave generation by prevailing westerly winds over a fetch of about 80 km . The shape and orientation of the bay opening to the west favors the accumulation of frazil and the consolidation of ice that drifts eastward along the south coast, which is exposed to the wave action.

The depth of Baie du Ha! Ha! is about 18 m at its mouth and gradually decreases towards the beach. The water level is modulated by semi-diurnal tides whose amplitude can reach 2.3 m (tidal range of 4.6 m) during spring-water. The thickness of the ice in the bay has been measured several times during several ice canoe mission in February 2016 and is 0.6 ± 0.2 m. The belvedere of a mountain adjacent to the bay, the Pic Champlain, was chosen to observe the sea-ice interactions.

The Pic Champlain is a 351 m-high nearby hill that overlooks the bay and allows for a clear wide view on the bay as well as on the offshore environment. Camera observations were obtained with a Erdman's Nano Biscuit All-In-One Time Lapse system, with a 20 MP Canon EOS 6D 20 MP SLR Digital camera mounted with a EF 17-40mm f/4L USM Ultra-Wide Zoom Lens and dual redundant 124 GB flash storage units. Each year, it was installed in late autumn or early winter on the wooden platform of the Pic Champlain belvedere (48°19'47"N, 68°50'04"W). The camera was set up every winter from 2014 to 2017. It is powered by batteries connected to 60 W solar panels and it is set to take a picture every two minutes between sunrise and sunset. The system is managed remotely with a 3G modem connection and enables changing the start and end times of the capture as the day duration lengthens from January to March. An image was sent every day to monitor the system as

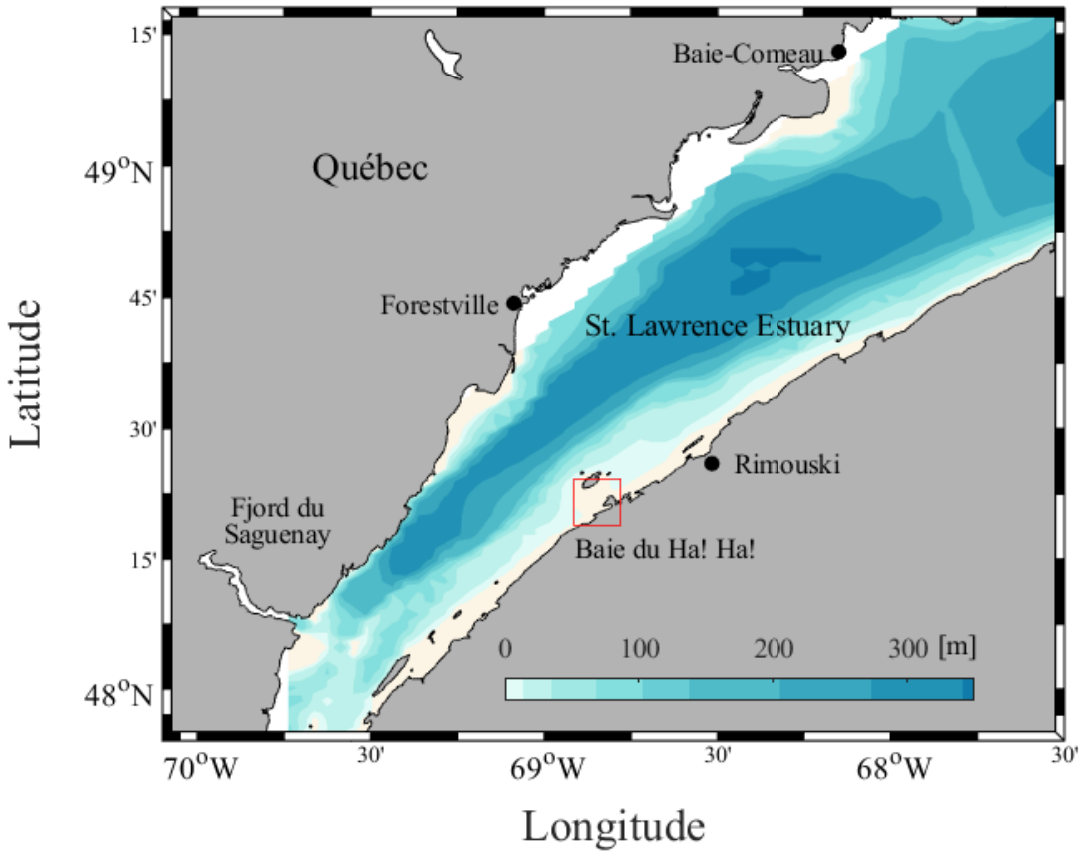

Figure 8: The Estuary of St. Lawrence, Canada. The red square indicates the location of Baie du Ha!Ha! in the Bic National Park near Rimouski, Québec, Canada.

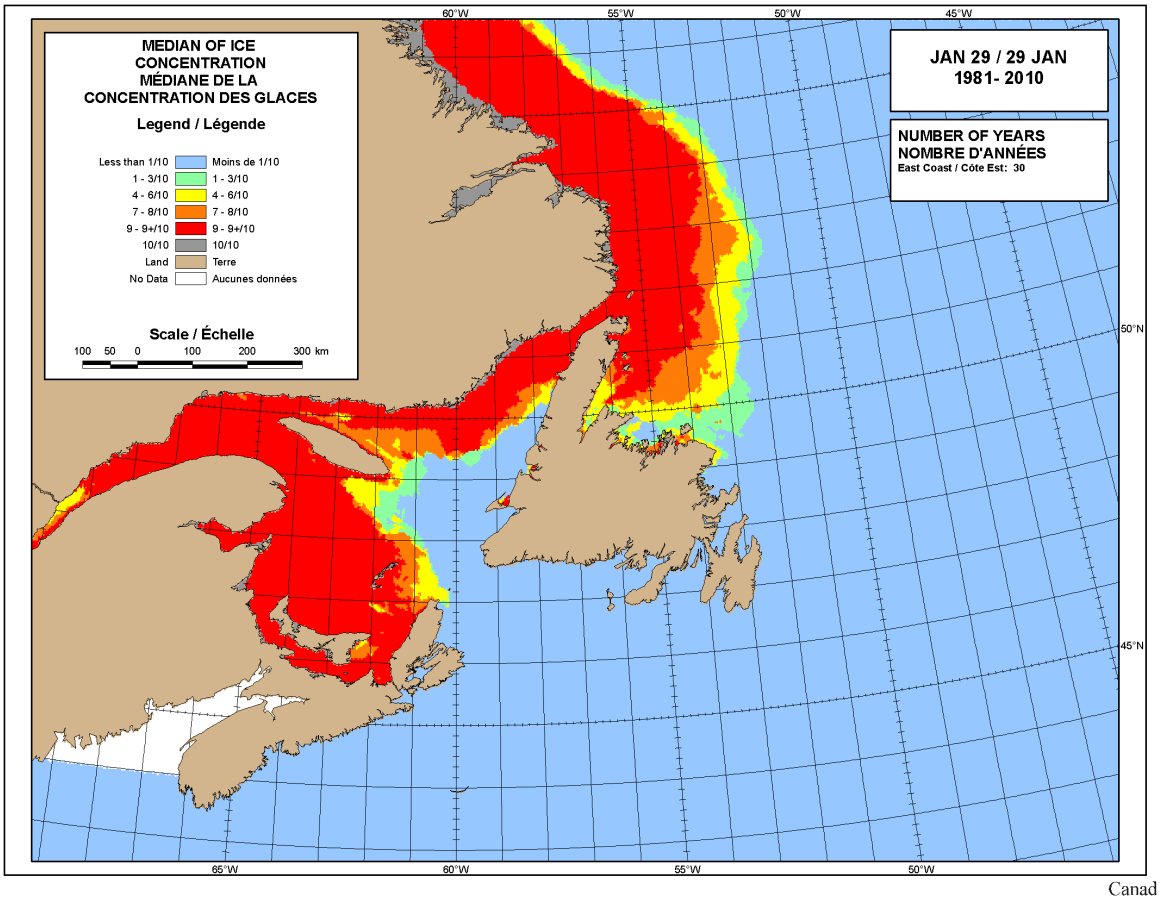

Figure 9: Map of the ice concentration over a 30-year period (1981-2010), produced by the Canadian Ice Service, showing a negative anomaly at the head of the Laurentian Channel (see Figure.8), near the mouth of the Saguenay River.

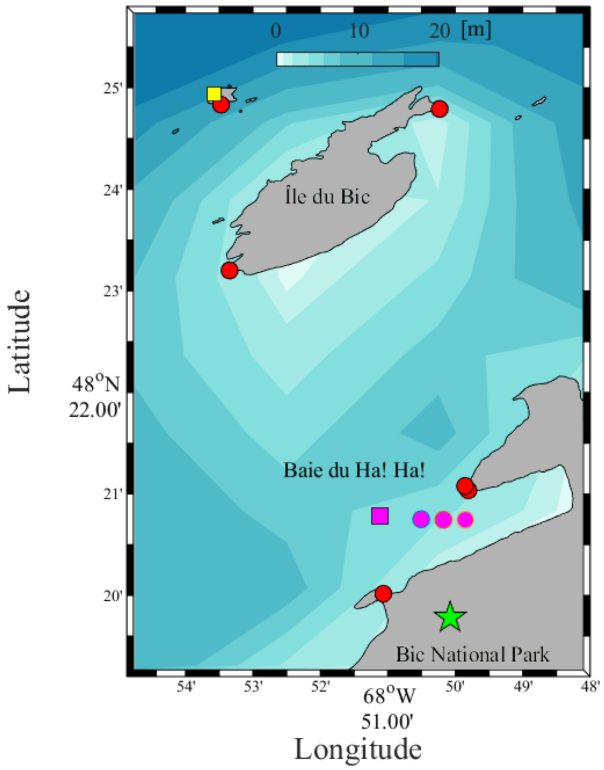

Figure 10: Map of Baie du Ha! Ha! showing the location of the camera (green star), ground control points used for image georectification (red circles), the Acoustic Wave And Current (AWAC) profiler (magenta square), the pressure gauges (magenta circles) and the Île Bicquette weather station (yellow square). The depth of the bay is less than 8 meters.

Table 1: Meteorological conditions (wind speed, direction and air temperature) given by the Île Bicquette station (WMO 71385).

Events	Date	$\lvert\mathbf{U}_{10}\rvert$ (km h^{-1})	θ (°)	T_{air} (°C)
A	January 28, 2014	45	210	-14.5
B	February 13, 2014	32	210	-5.1
C	January 28, 2016	25	210	-5.5

well as the coastal environment and the visibility.

Approximately two to three events have been completely or partially observed each year, but because of the visibility, only three events have been sampled well enough for analysis in the present work. The first event happened on January 28, 2014 (A), the second on March 13, 2014 (B), and the third one on January 28, 2016 (C). In 2016, an AWAC (AWAC-AST 1 MHz) and three pressure gauges (TWR-2050) were deployed and recorded informations about waves and current (see section 2.3.1). For the 2014 events, no in situ information were collected about waves, but the wavelength of event B was extracted directly from the images. The methods used for extracting wave conditions are discussed in section 2.2.5. The meteorological conditions for the events are contained in Table 1.

2.2.2 Georectification

In order to extract quantitative informations from oblique images, georectification must be performed first. We use the algorithm `g_rect` based on Pawlowicz (2003) and developed by Bourgault (2008). Ground control points at sea level, for which we have a good knowledge of the latitude and longitude coordinates, must be clearly visible on the pictures (Figure 11). The georectification algorithm maps pixels onto a regular longitude-latitude grid, stretching the pixels depending on their location on the picture. The effective resolution spans from 2 m on the southern coast of the bay to approximately 6 m at its mouth on the opposite side,

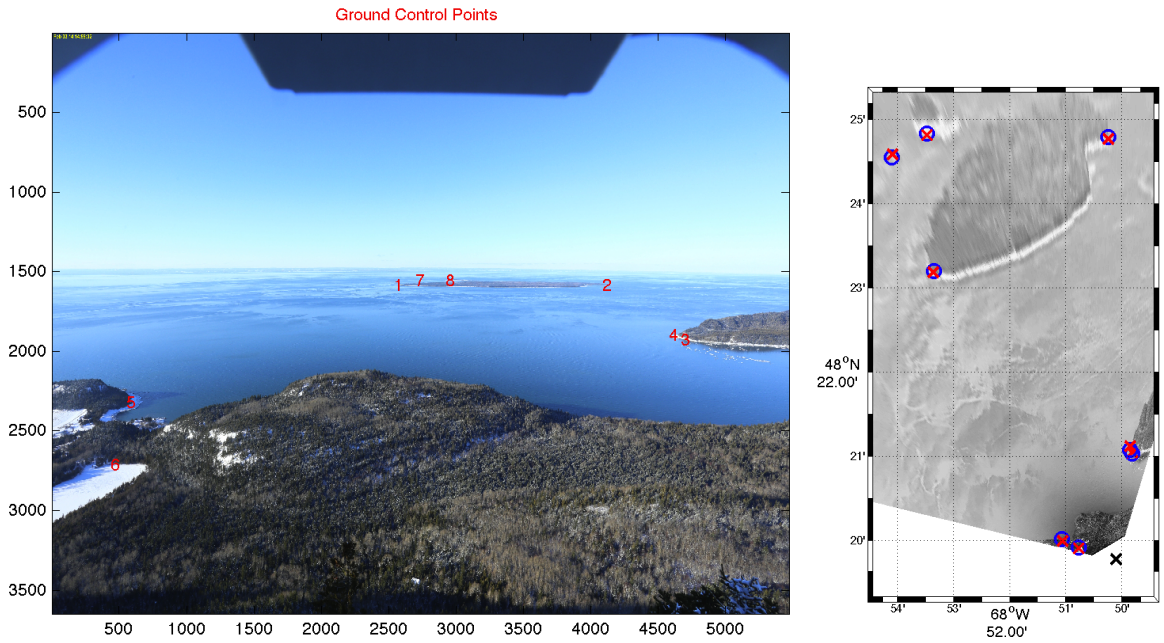

Figure 11: **Left**: The raw oblique picture taken by the camera during a clear day with the red numbers showing the location of the eight ground control points (GCP). **Right**: The corresponding georectified image obtained by minimizing the root mean square distance between GCPs and their estimated location.

which corresponds to the main area of interest where results are obtained and analyzed (see Figure 13) . Oblique images are then interpolated on a regular grid with cells of 0.5 m in order to use image processing tools and resolve the smallest floes. Examples of georectified images for the three events are presented in Figure 12.

2.2.3 Sea ice deformation

The particle image velocimetry (PIV) is a method that yields the velocity vector field of markers contained in a fluid using the cross-correlation function between a pair of images separated by a short time lapse. The PIV method is hereby used to extract the motion of ice floes and to describe the marginal ice zone dynamics. We use the PIVlab 1.41 Matlab toolbox

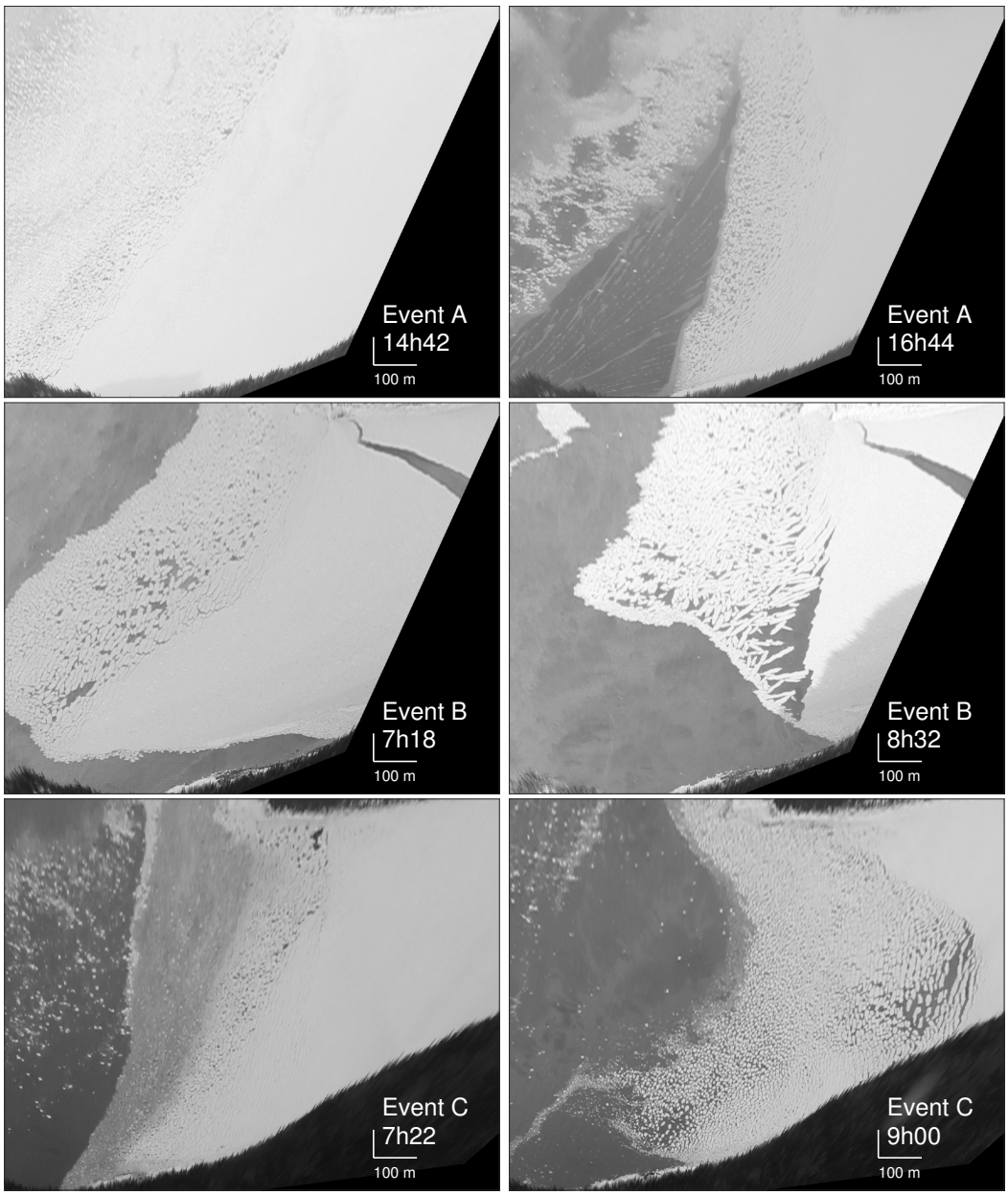

Figure 12: Examples of georectified images taken at the beginning and at the end of each of the three events. The image taken at 14:42 during event A is blurred because visibility was reduced at this time.

(Thielicke and Stamhuis, 2014) with an interrogation area, which is defined as the smallest square area that will be used by the cross-correlation, of 80×80 pixels with an overlap of 50%. This yields a smoothed velocity field with a resolution of 40×40 pixels (20 m $\times$ 20

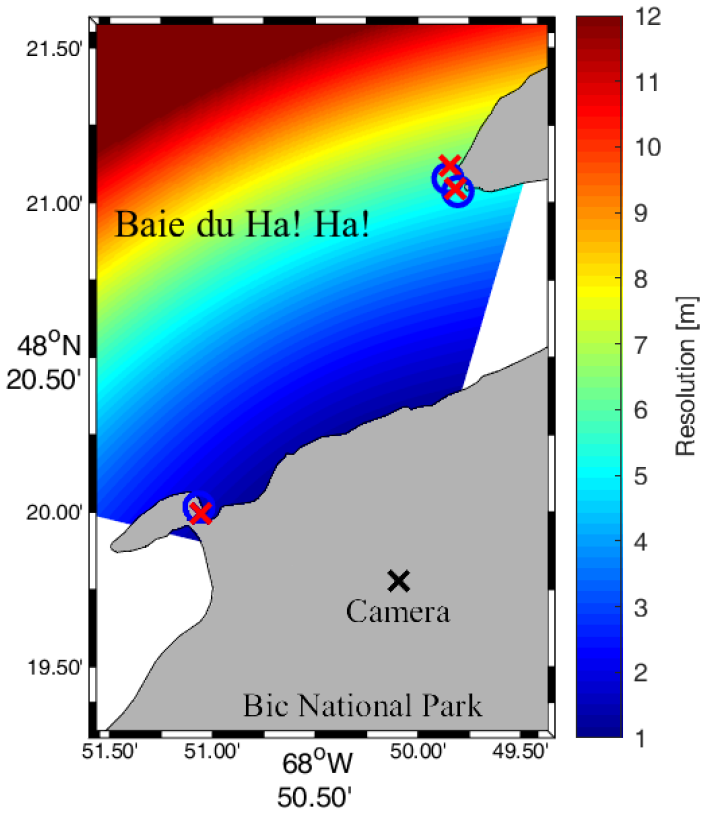

Figure 13: Effective resolution of the camera at the mouth of the baie du Ha! Ha!.

m). A test is run over the final vector field so that every vector is compared to the median of its direct neighbors. If its value is above seven times the standard deviation, the vector is removed and replaced by a linearly interpolated estimate. An example of PIV analysis is presented in Figure 14.

In order to describe the evolution of the ice morphology as a function of time only, we adopt a lagrangian framework and measure properties of the same ice volume, assuming there are no losses or gains throughout its journey in the marginal ice zone. For this, we use the velocity field obtained with the PIV method and apply it to an initial mask. We proceed by selecting the vertices of a polygon circumscribing the area of interest. The size and location of the polygon are selected so that it will ultimately enclose a large number of floes, in order to optimize the significance of statistical properties, and that it will remain within the image domain during the entire event. Each vertex is advected using the velocity field of the PIV velocity linearly interpolated at the vertex position, a procedure that defines a time-dependent mask. Since the velocity field is not homogeneous, the mask may deform or rotate.

2.2.4 Floe size distribution

To separate ice from liquid water, the RGB image is transformed into an intensity image where the intensity I is defined as the average of the R, G and B values (Figure 16a). After the contrast between ice and water is adjusted (Figure 16b), an intermediate intensity value $I_c(n)$ is manually selected between the intensity of ice $I_i(n)$ and the intensity of water $I_w(n)$ for each image n. This simple threshold criterion is then used to create a binary image where $\tilde{I}(I \geqslant I_c) = 1$ and $\tilde{I}(I < I_c) = 0$, which can then be used to extract information about ice floes. Since the raw and adjusted intensity vary with time during the day, one threshold value can not be used for all images and all events, and this step requires manual optimization from trial and error. But even in lighting ideal conditions of light, this criterion can not separate floes that are very close to each other because of insufficient resolution or floes in direct contact. This is why an additional step is required to separate floes. For this, we use the

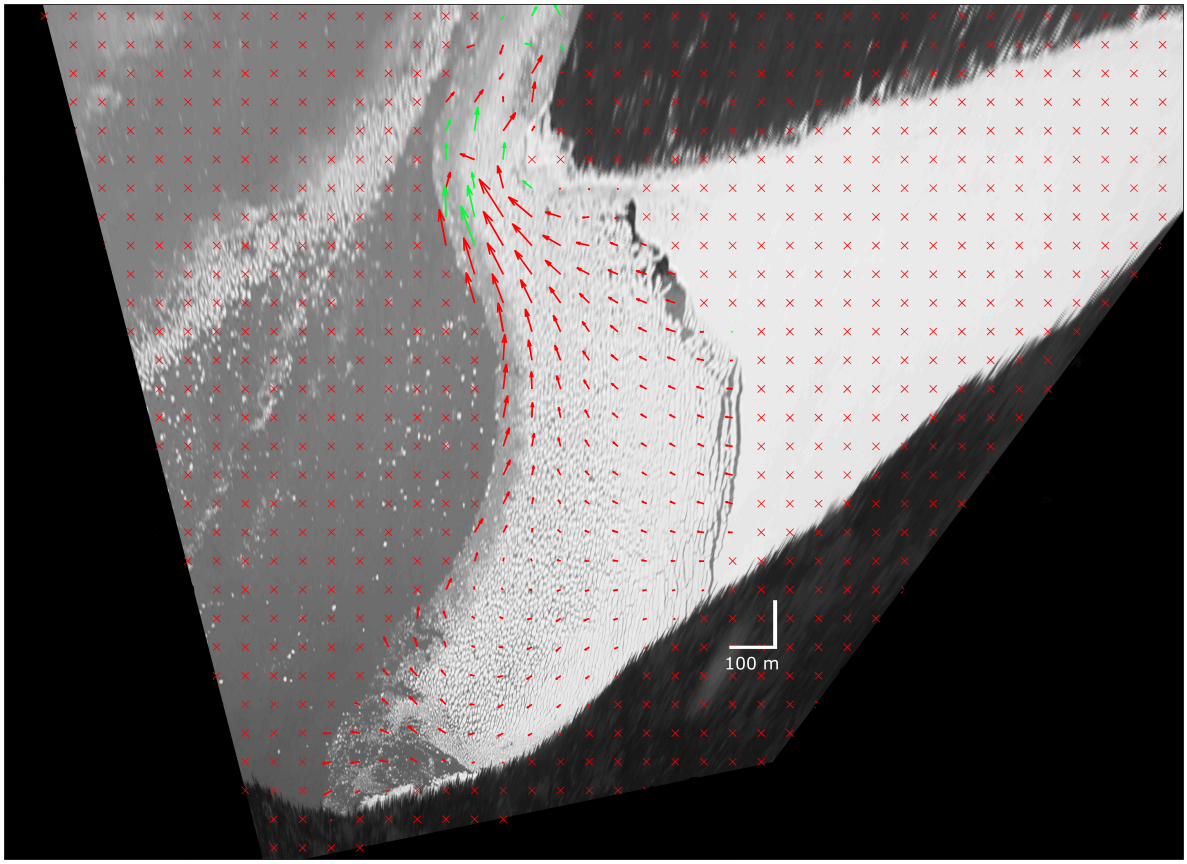

Figure 14: Example of PIV results obtained with PIVlab 1.41 for the images taken on January 28, 2016 at 8h20 and 8h22 am. The vector field is displayed over the 8h20 picture. Each red vector represents the mean displacement velocity of cell 40×40 pixels. Crosses indicate cells with no value because of a handmade mask over those regions. Only one vector over two is displayed for clarity. The red ones are the results of the PIV cross correlation algorithm and the green ones are the results of interpolation over the outliers. Spurious variations in vector field in the northern part of the picture are discussed later.

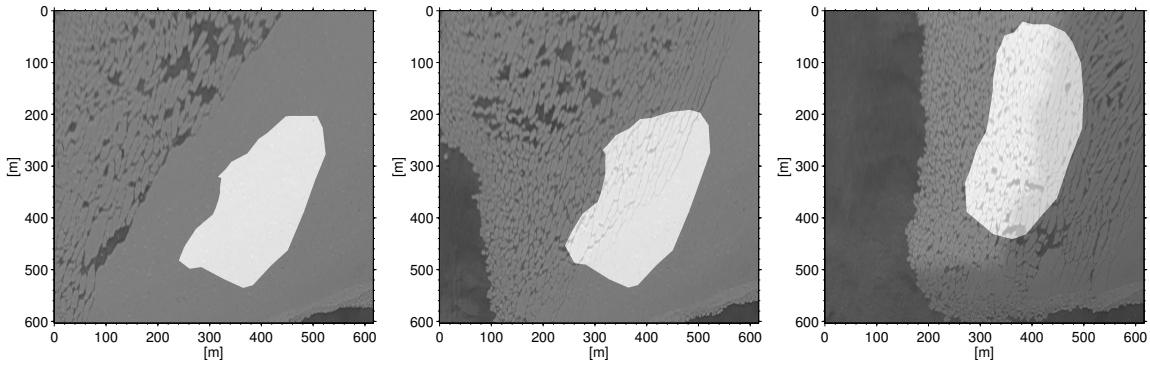

(a) 07h12 EST (b) 07h32 EST (c) 07h52 EST

Figure 15: The mobile mask at three different times (07h12, 07h32 and 07h52 am EST, respectively) during the break-up event B. The deformation and advection of the mask are clearly visible on that sequence of images.

watershed method that treats binary shapes as topographic surfaces where the elevation is the closest distance between a point and a boundary. Floe centers correspond to local maxima which, if in contact, will be separated by a local minimum value. A threshold value manually determined from trial and error to avoid over-segmentation or sub-segmentation is selected to draw a line along the lowest elevation path between two local maxima: the watershed valley. For quantitatively analyzing the floe size distribution and to minimize the impact of random motion in the image processing, three images taken at two-minute intervals are clustered into one average point. Binary shapes with an area less than six pixels are removed since this is considered as the limit of detection. Floes are considered full and water pixels inside them are filled. The whole process is shown in Figure 16.

2.2.5 Wavelength

Wave parameters for event C are extracted from the AWAC (see section 2.3.1). Since the waves are clearly visible on some images of event B, it is possible to extract the distance between the wave peaks λ by measuring the distance between wave crests. But in order to

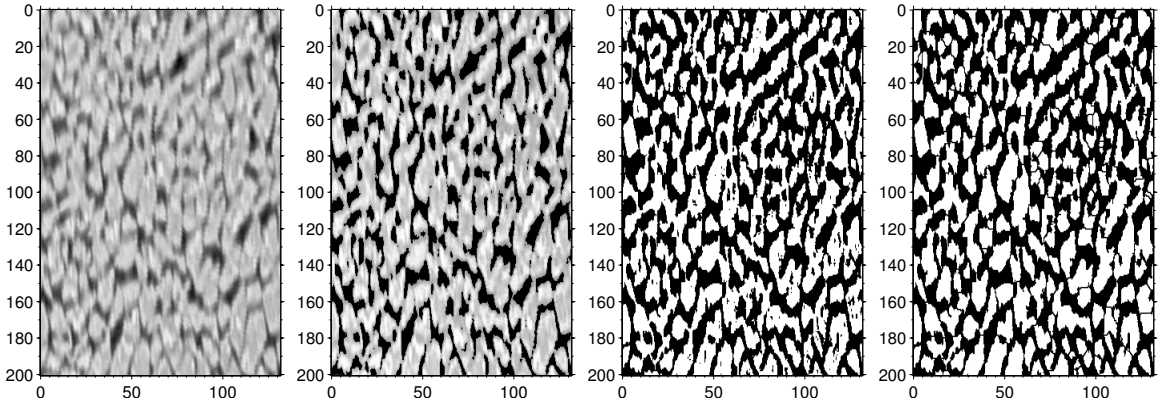

(a) RGB intensity (b) Contrast adjusted (c) Binary image (d) Segmentation and filling

Figure 16: Four steps of the image processing on a high density of floes region. a) *RGB* values are averaged to obtain a grayscale image of the intensity I, b) contrast is adjusted, c) the binary image is constructed with the threshold criterion and d) the final result after the watershed segmentation has been applied and the floes have been filled in order to remove the small holes associated with raw on the images.

improve the accuracy and decrease the number of measurements made directly on the images to determine the wave wavelengths, the 2D fast Fourier transform was used. With this method, it is possible to know more precisely the wave spectrum and its direction. The 2D Fourier transform, when applied to a portion of the image where a wave field is clearly visible, analyzes the periodicities present in the image and produces a 2D spectrum composed of spatial wavelengths. In practice, it is sometimes difficult to distinguish the clouds of points associated with the waves in the spectrum. In addition, if objects (coast, floes, light reflection, etc.) are present, edge effects, often present when making the Fourier transform image, dominate the spectrum. Nonetheless, this method was used to extract the wave modal wavelength present in some clear images of event B.

2.2.6 Uncertainties

Algorithms described earlier come with uncertainties. In this paper, without any other in situ observation, the human eye is considered as the ground truth which is used to assess errors of the method. To have an estimate of the errors made by the watershed method, a comparison between three zones with floes identified by human and the same zone treated by the algorithm was performed. The difference in the number of floes is around 10 % depending on the zone of interest. Algorithm results show an overestimation of the number of big floes. First, because it is difficult to separate floes in contact without having over-segmentation. A closer look at Figure 16d shows examples of irregular shapes with many concavities caused by floes in contact. They are hard to break-up without over-segmenting other floes. Second, by assuming that floes in contact can separate from one another between two pictures (120 seconds), it is also possible that other floes, that were not in contact in the first image, enter in contact in the second or third image. This results in an overestimation of the biggest floes at the expense of the smallest.

The total surface of ice in the mobile mask changes over time (see Figure 17) even though it should not, in principle, since the mask follows the total ice area. Around 25-30% of the ice present in the mask is lost during each event. There are many reasons that can explain this observation. First, floes drift from a high resolution to a low resolution portion of the image, which can increase the number of floes that are too small to be resolved and detected by the camera (referred to as dark ice by Zhang and Skjetne (2015)). This phenomenon is amplified by the fact that more small floes are produced by fragmentation. Secondly, floes that are covering 6 pixels or less (1.5 m^2) are not considered by the algorithm because they are too easily confused with noise. Third, the most important factor is the threshold criterion I_c during the process. A change in this parameter changes the total ice seen by the algorithm. Sensitivity tests have been performed and a 5% change of the I_c value (the threshold value determined by eye to yield the closest result to reality) can generate a change in total ice seen by the algorithm of up to 15%. The difficulty to isolate small floes in contact causes the image

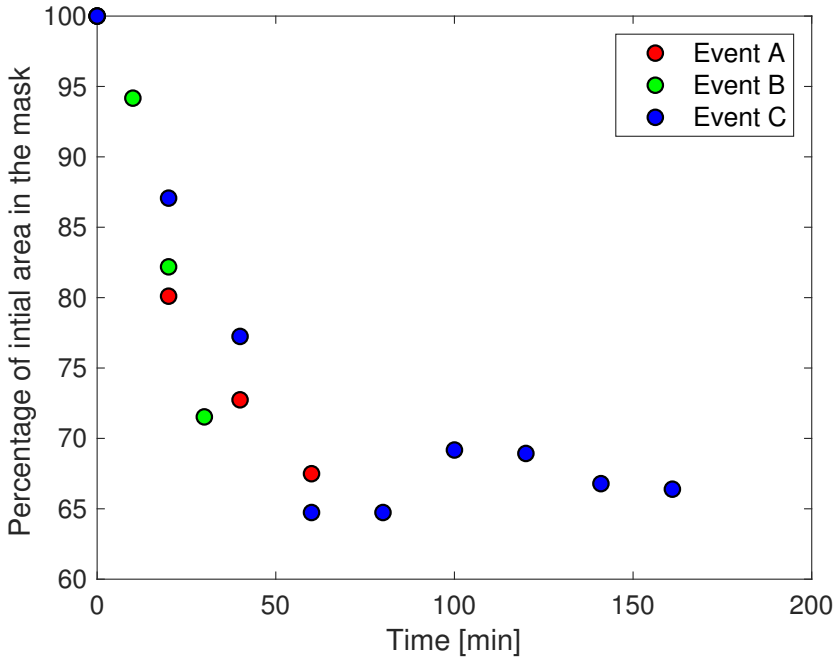

Figure 17: Surface area of the mask that is covered with ice during the event. The first mask is the reference so they all start at 100%. The event C is the only one that seems to converge between 65% and 70%, but it is also the only event to reach a equilibrium state (see 2.3).

taken later during break-up to have higher threshold criterion and is thus partially responsible for the loss of total ice. This loss of ice surface during the events thus results from natural processes (some pieces of ice fall into the water during the break-up or during collisions), but also from the algorithm and the resolution of the picture.

The PIV analysis made with PIVlab 1.41 gives quantitative results of what the human eye sees from picture to picture except in the northernmost part of the domain where the resolution is the lowest and where patterns are blurry. Flow aberrations are visible on many images (Figure 14), so this part of the images were avoided in the analysis.

2.3 Results

In this section, we present wave and current conditions, and the evolution of the floe size distribution, and floe morphology for each event. We also present the ice edge progression, the deformation fields and their relations with the floe size and concentration. An emphasis on event C is made since it is the most complete in terms of data coverage.

An important assumption in this paper is that waves are the main cause for ice break-up. The first observation that supports that hypothesis is that in all events, floes that detach from the ice pack have an elongated shape (rod-shaped floes), i.e. they have a large isoperimetric ratio. During event B, when surface waves are clearly visible, rod-shaped floes are first created and, as they rotate with the current, they are broken up in smaller isotropic floes. At some point, waves die out and these rod-shaped floes keep their elongated shape even if they have rotated (see Figure 18b).

Another visual observation on Figure 18 is the large crack present in the top-right corner of the picture. This crack does not move during the event B and the ice edge never reaches this lead. This shape and location is indicative of a plastic failure of the ice plate possibly due to a tensile stress caused by the outward current. Waves at this location in the ice have long been attenuated. It highlights in a single picture a rheological distinction between wave-induced fragmentation and current-induced failure, which will be discussed in section 2.4.

2.3.1 Wave conditions

Except for the camera, no device that could give information about the waves was deployed in the bay during the winter of 2014. During event B, two different wave fields are visible on the images with different modal wavelength and orientation (Figure 19). The shorter waves have a modal wavelength $\lambda_p = 12 \pm 2$ m and are obtained with the Fourier analysis. The larger waves captured by the camera have a modal wavelength $\lambda_p = 24 \pm 5$ m,

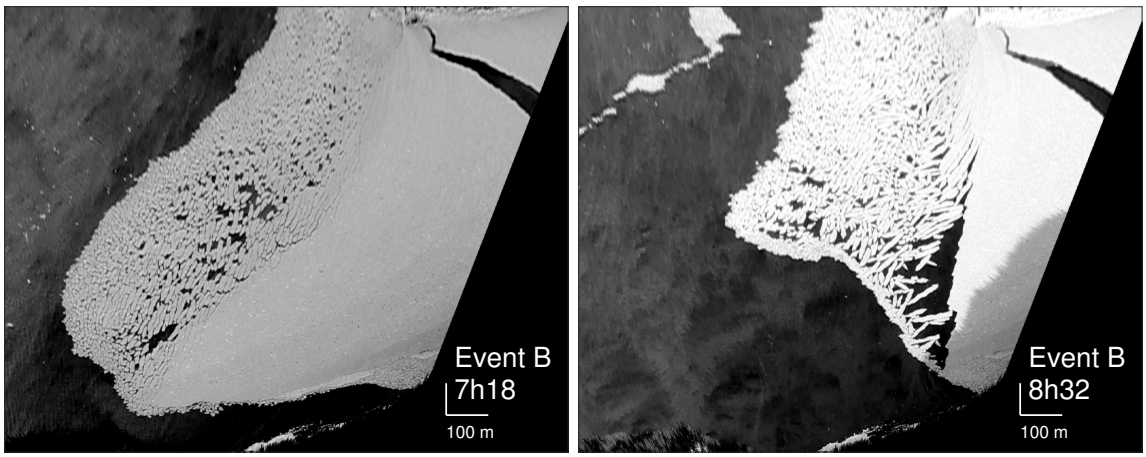

(a) 7h18 (b) 8h32

Figure 18: a) At the beginning of event B, surface waves are clearly visible on the left side of picture. Rod-shaped floes created near the ice edge are progressively broken up in smaller isotropic floes over time. b) At the end of the event, no wave is visible and rod-shaped floes are not broken up anymore as they drift. Some rod-shaped floes are rotating and some are even perpendicular to the earlier incoming waves.

which was estimated visually from the pictures since they are too blurry for the FFT algorithm. For event C, the data from the AWAC and the pressure gauges are shown on Figure 20. It is important to note that the break-up event occurs between 7h00 and 9h00 EST, but at that moment, the energy of the incident waves is not particularly important in comparison to the night before the event. The dominant wavelength measured over the 24 hours preceding the break-up was approximately 30 m while during the break-up it was between 25 ± 5 m. The surface current is shown in Figure 21. The fragmentation event C captured by the camera coincides with the moment where the current is oriented towards the bay with its maximum velocity. Note that the AWAC is outside the bay and does not describe the dynamics inside the bay. The wavelength and the orientation of the modal wave phase front for all three events (θ_{wave}) are presented in Table 2.

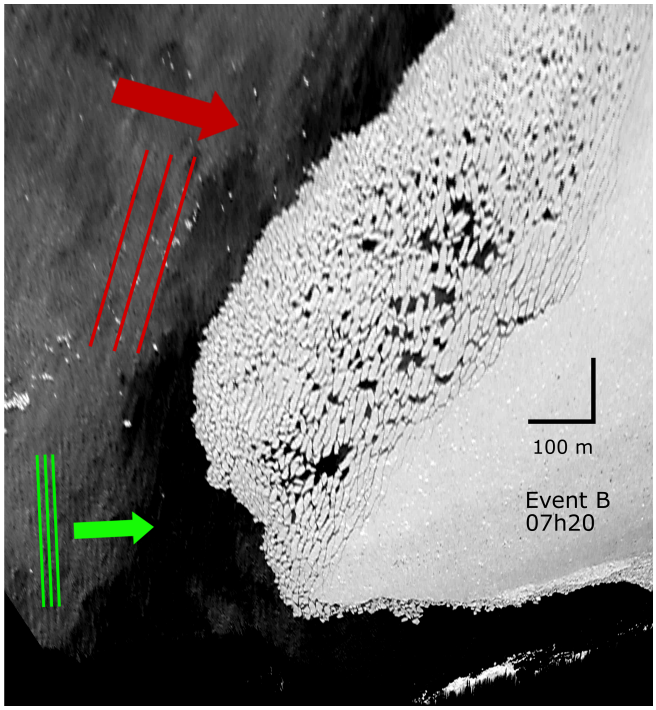

Figure 19: Zoom in a region where the wave fields are visible during event B. The green one is measured with the Fourier transform. The red one, more difficult to see on the figure, is measured directly on the pictures.

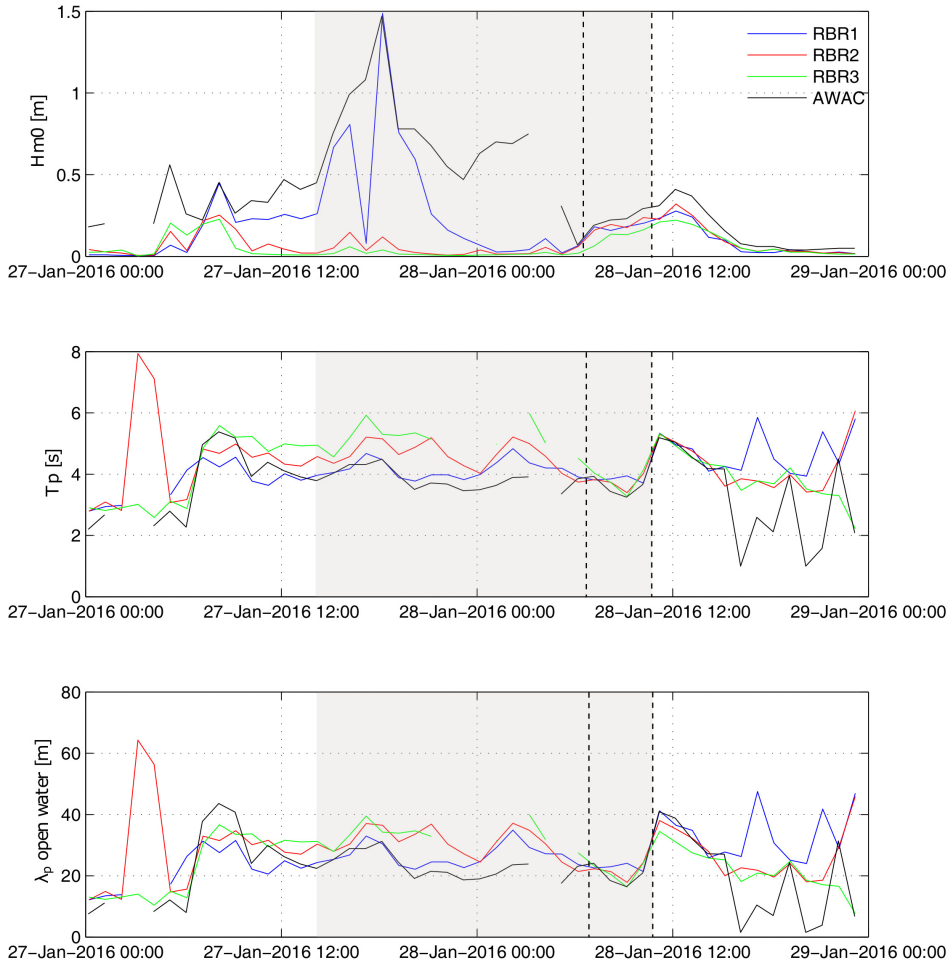

Figure 20: Significant wave height H_{m0}, peak period T_p and peak wavelength λ_p obtained from the AWAC and the pressure gauges. The dashed lines delimit the interval during which the fragmentation is captured by the camera. An energy peak is captured by the AWAC more than 12 h before. The AWAC can not measure waves when there is sea ice in its detecting radius while pressure gauges can.

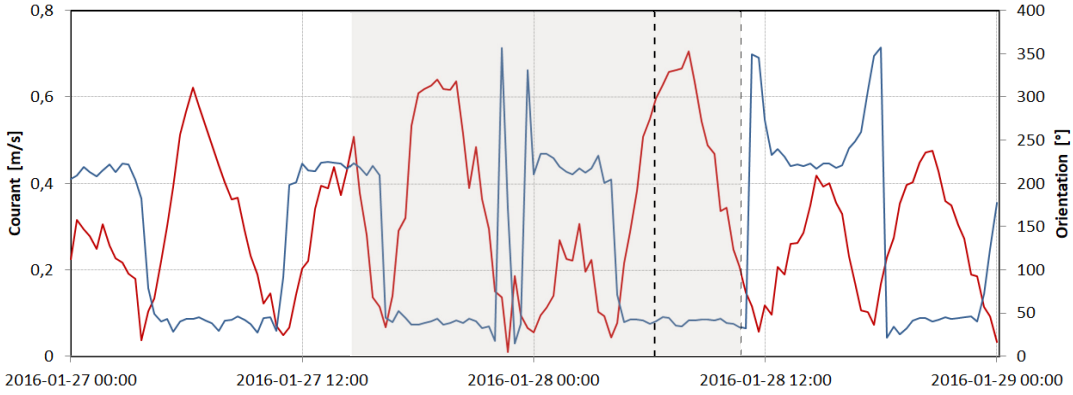

Figure 21: Current speed (red) and its orientation (blue) measured by the AWAC for the event C. The dashed lines indicate the interval during which the fragmentation event is captured by the camera.

2.3.2 Orientation of waves and cracks

In order to compare the incident wave front with the orientation of the cracks in the landfast ice, the orientation of the largest, rod-shaped floes breaking up from the ice pack has also been measured by approximating those floes as ellipses. The angle θ_{minor} presented in Table 2 corresponds to the orientation of the minor axis of those ellipses. In principle, the minor axis is roughly perpendicular to the cracks shortly after the first break-up, and parallel to the wave propagation direction. Since the minor axis of an ellipse is not a vector (it has no direction), we force $180° < \theta_{\text{minor}} < 360°$.

The longer waves in event B are considered to be the cause of ice cracks because of their orientation parallel to the cracks and because crack spacing $\tilde{D}_{\text{ice}}$ is nearly half of their modal wavelength. The percentage deviation of θ_{minor} from θ_{wave} is 2% for event B, if we consider the larger waves to be responsible for the fragmentation, and 8% for event C.

Table 2: This table shows values of θ_{wave} and θ_{minor} for all three events. The orientation of the ellipse (minor axis) is defined to be between 180° and 360°.

Event	λ (m)	θ_{wave} (°)	θ_{minor} (°)
A	-	-	290 ± 20
B	24±5[a]	295±20[a]	290 ± 20
	12±2[b]	260±10[b]	
C	25±5[c]	260 ± 20[c]	280 ± 20

[a] Visual inspection of the images.

[b] 2D Fast Fourier Transform.

[c] AWAC.

2.3.3 Time-resolved floe size distribution

Instead of binning floe sizes into arbitrarily pre-determined categories as done, for example, by Herman (2010), the floe size distribution is calculated as the normalized cumulative floe area distribution (ϕ) obtained by ordering floes from the smallest to the largest, by summing their area and by dividing by the total ice area. For a given event, ϕ is computed for each image using floes enclosed in the mask, ultimately providing a time-evolving FSD for a small portion of the ice cover. Figure 22 shows the time-dependent ϕ for the three events. The selected zones for the analysis are initially located in the ice pack, i.e. within the landfast ice prior to the break-up. Over time, this initial ice pack breaks up into smaller floes as waves propagate and bend the ice plate.

Floes drift away after the initial break-up and are further broken up in smaller pieces as the ice opens up and waves continue to act on them. The fragmentation of the biggest floes into smaller ones increases the fraction of area occupied by small floes. One very interesting observation from Fig. 22 is that the distribution changes significantly during the initial break-

Table 3: This table displays the $\tilde{D}_{\text{ice}}$ (m) and $\tilde{D}_{\text{stable}}$ (m) measured manually for all three events. The standard deviation of the measures is also included in the table.

Event	Date	$\tilde{D}_{\text{ice}}$ (m)	$\tilde{D}_{\text{stable}}$ (m)
A	January 28, 2014	9.7±1.6	7.2±1.0
B	February 13, 2014	11.8±2.1	8.5±1.3
C	January 28, 2016	11.6 ±1.7	7.4 ±0.7

up of the ice pack, but seems to reach a stationary state. This state is interpreted as a stable equilibrium during which no break-up occurs anymore (or much less often than before). In order to determine the most dominant floe size in the MIZ at equilibrium state (the mode of the distribution), called A_{p}, the derivative of the last three curves of the ϕ has been taken for event C (Figure 23). This graph shows the fraction of the total area occupied by floes between A and A+dA. . A_{p}, which corresponds to the maximum of Figure 23, is represented by the dash line on Figure 22. A_{p} is equal to 40 ± 7 m^2 and the effective diameter of the dominant floe size is $D_{\text{p}} = \sqrt{40} = 6.32$ m.

For each event, the very first cracks in the ice pack are somewhat parallel (see section 2.3.2) to the wave phase plane and floes are mostly elongated. The distance between these initial cracks depends upon the failure mechanism (flexural stress induced by the waves, as described in 2.1) and is called $\tilde{D}_{\text{ice}}$. This characteristic size can be compared to the size of the biggest floes when an equilibrium state is reached, called $\tilde{D}_{\text{stable}}$. $\tilde{D}_{\text{ice}}$ and $\tilde{D}_{\text{stable}}$ have been measured manually directly on the pictures for all events. In order to measure $\tilde{D}_{\text{ice}}$, the size of 30 floes, not necessarily contained in the mobile masks, that separated from the ice pack at different moments has been measured. Similarly for $\tilde{D}_{\text{stable}}$, the size of 30 of the biggest floes was measured once the equilibrium state was reached. This analysis allows to measure the maximum size for which the floes stop to break under mechanical forcing. Averages over many floes have been made for all events and are summarized in Table 3.

In order to characterize the floe evolution in relation with the waves, the equivalent

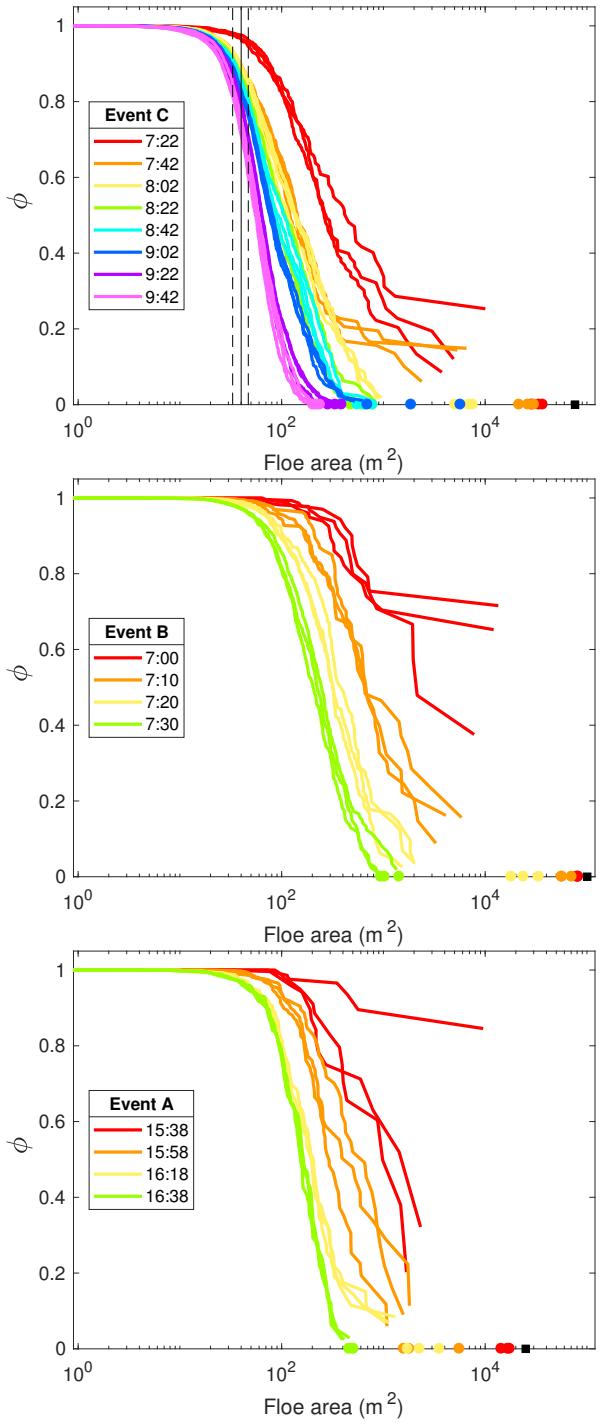

Figure 22: Time-dependent normalized cumulative floe area distributions (ϕ) for all three events. For event A and C, each curves are separated by 20 minutes and for event B, which is shorter, curves are separated by 10 minutes. The dash line on the event C graph represents A_p, the maximum of the last curves derivative (equilibrium state). $A_p = 40 \pm 7\ m^2$.

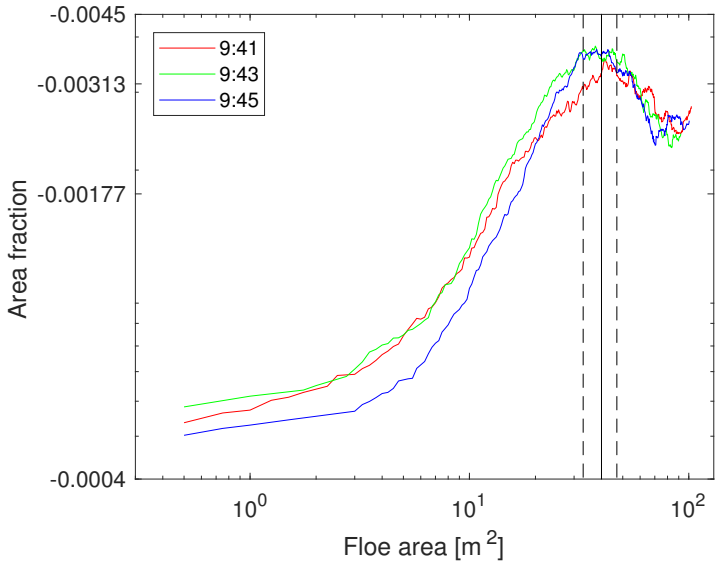

Figure 23: Derivatives of the last three profiles of ϕ for the event C. Those distributions correspond to the area fraction occupied by each floe size. The vertical lines represent A_{dom} and its uncertainties. They were manually drawn. A_{dom} is equal to 40 ± 7 m^2.

diameter of a circular shaped floe with the same area D_{eq} is calculated for the biggest floes in Figure 25. As shown in Figure 24, the circular shape is at first a rough approximation of the real shape of the biggest floes (although it is used in collisionnal models), but D_{eq} is another indicator of the evolution of the biggest floes in the MIZ. D_{eq} does not show a clear convergence over time to one specific value. At the end of the event, D_{eq} is at 9.0 ± 0.5 m. For this calculus, only the 70$^{\text{th}}$ to 90$^{\text{th}}$ percentiles were considered in order to avoid errors associated with floes in contact.

2.3.4 Floe morphology

Figure 26 shows the number of floes per square meter and the total perimeter of each floes per square meter as a function of the number of waves that have crossed the MIZ. The number of floes and the perimeter were divided by the initial area of ice present in the first mobile mask in order to compare the events. The number of floes and the total perimeter is dependent on the quantity of ice, which is very different for events A, B and C.

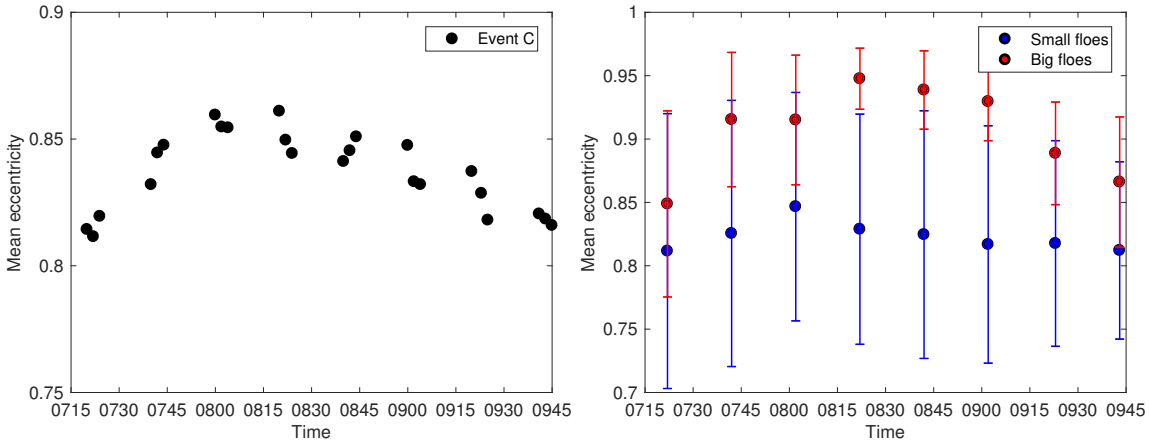

Figure 24: Mean eccentricity of all floes within the mask as a function of time (left) and the mean eccentricity for 70% smallest floes the 30% biggest floes (right). The error bars correspond to one standard deviation.

A normalization is done to link the evolution of those parameters to the waves, which are the main drivers of the evolution of the FSD. τ, is defined as

$$\tau = \frac{t}{T_{\mathrm{MIZ}}} \tag{2.5}$$

where t is time and T_{MIZ} is the time needed by the waves to cross the MIZ, defined as

$$T_{\mathrm{MIZ}} = \frac{L}{c_g} \tag{2.6}$$

where L is the average MIZ width (here taken as 500 m) and c_{g} is the group speed

$$c_g = \frac{1}{2} c_p \left(1 + \frac{2kH}{\sinh(2kH)}\right) \tag{2.7}$$

with $c_{\mathrm{p}} = \lambda/T$ is the phase speed and H is the water depth. The wavelength λ and the period T are extracted from Figure 20. Since no wave information is available for events A and B, except λ of event B, which is very similar to event C, data from event C are used to compute τ which is assume to be the same for all three events. For event C, both the number of floes

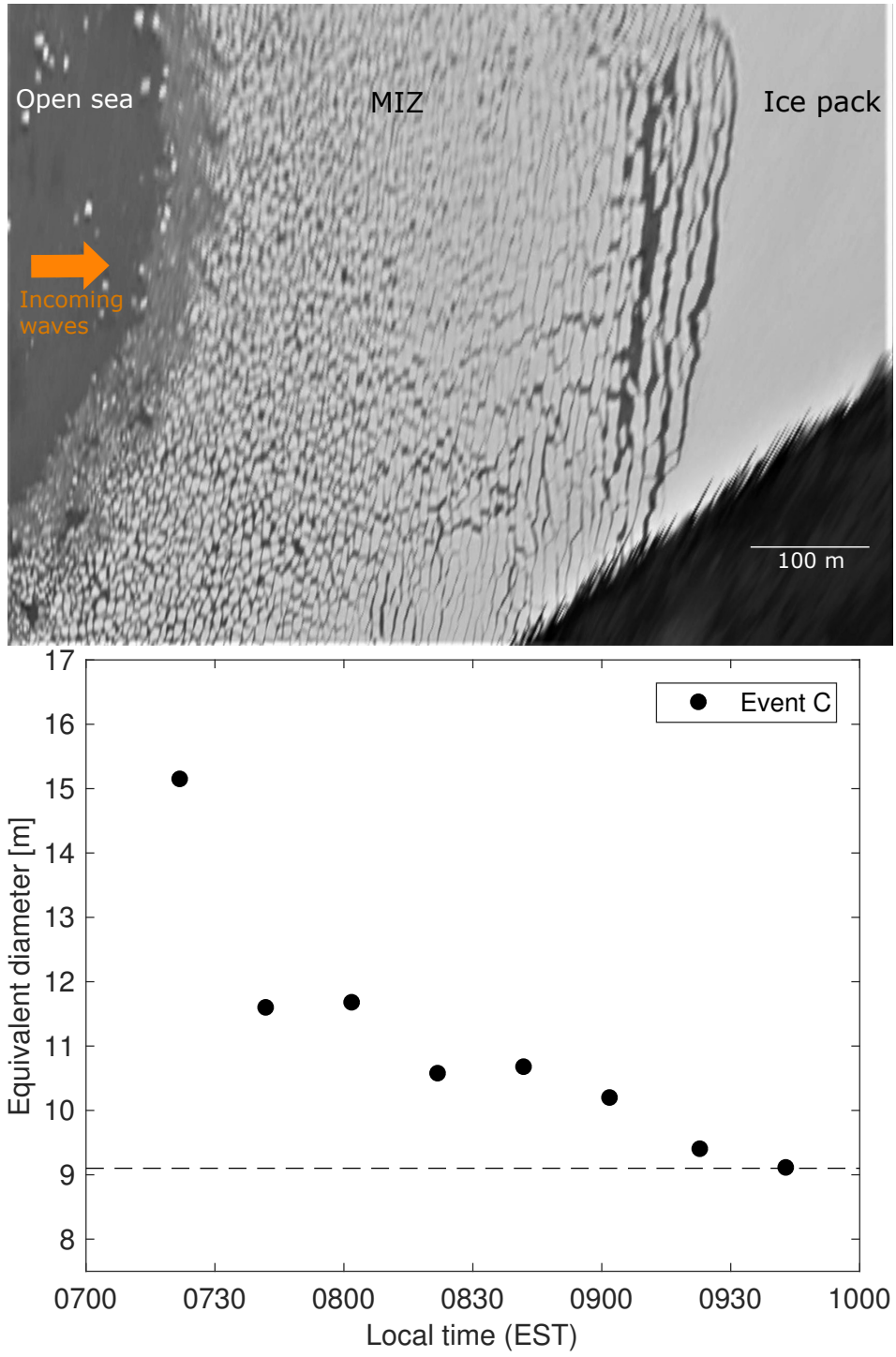

Figure 25: a) Zoom of a grayscale, contrast-adjusted image taken at 8h34 during the event C is displayed. Unbroken ice pack is on the right and the ice-free water is on the left. A floe size gradient is present between free water and the rod-shaped floes that just broke are clearly visible near the ice pack. b) Evolution of the equivalent diameter D_{eq} for event C. Each point represents the average of three consecutive images. The dash line represents the value of the last trio of images $D_{eq} = 9.0 \pm 0.5$ m.

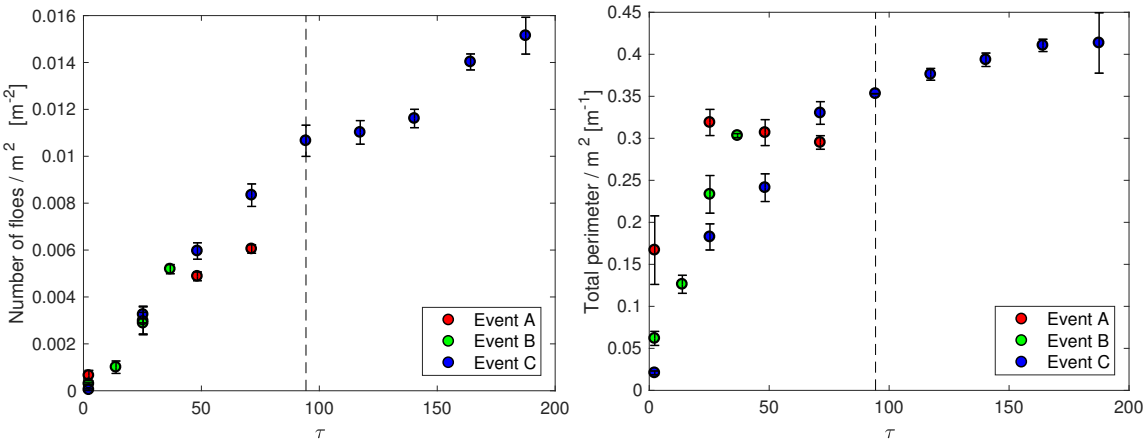

Figure 26: The total number of floes (left) and perimeter (right) normalized by the initial ice area as a function of τ for event C. The dash line represents the approximate moment when the initial ice pack is completely broken. The error bars are the standard deviation of each sequence of three images.

over time and the total perimeter seems to show a small change of regime, indicated by the vertical dash line on Figure 26. It corresponds to the moment at which all ice in the mask has broken up from the landfast cover and starts to drift away, which is determined visually from the pictures for the event C only. Before that moment, the distribution seems to increase rapidly and linearly, like in the events A and B. The second regime, much smoother, shows a lower increase of the number of floes and total perimeter over time.

Figure 24 shows that the mean eccentricity (ratio of the distance between the foci of the ellipse and its major axis length) evolves over time. When the floes are divided in two groups, the 70% smallest present in the mask and the 30% biggest. The mean eccentricity does not behave the same way for both groups. Once again, only the event C is taken for this analysis since events A and B do not reach equilibrium. At first, the eccentricity is almost the same for the big and small floes (there is only a few floes broken). At the end of the event C, it is again almost the same but smaller floes's eccentricity remain almost constant over time and the big floes experience an increase of eccentricity followed by a decrease.

Another way to link the eccentricity and the size of the floes is presented in Figure 27. In this figure, the eccentricity of each individual floe in the events A, B and C is plotted as a function of their area. During those events, big floes are more elongated (eccentricity near 1), while small floes show a greater variability of eccentricity.

2.3.5 Ice edge

Figure 28a shows the progression of the landfast ice edge for each event. It is measured by taking the ice edge position from image to image along three lines. Figure 28a is an example of one image of the event C (8h30) for which the position of the ice edge has been manually identified (green square on the picture). Figure 28b is the average progression of the ice edge for all three events. The average speed (progression of the ice edge in the ice pack), given by the slope of the derivative, is 1.7 m s^{-1} for event A, 3.1 m s^{-1} for event B and 1.7 m s^{-1} for event C. An irregular progression of the ice edge is visible on Figure 28a. The ice edge experiences alternation between rapid break-up phases and pause phases. This becomes even clearer in Figure 28c, where the transects of event C are displayed and not averaged as in Figure 28b. It shows that the ice edge does not progress in the lanfast ice steadily.

2.3.6 Sea ice deformation

Many physical quantities describing the deformation of the ice are plotted in Figure 29 by using the u and v fields extracted with the PIV method. The calculation of those quantities are different components of the velocity gradient tensor $u_{i,j} \equiv \frac{\partial u_i}{\partial x_j}$ where $i, j = 1, 2$, which can be developed as a sum of a symmetric $\dot{\varepsilon}_{ij} = \frac{1}{2}(u_{i,j} + u_{j,i})$ and an antisymmetric part $\dot{\Omega}_{ij} = \frac{1}{2}(u_{i,j} - u_{j,i})$. $\dot{\varepsilon}_{ij}$ is called the strain rate tensor and $\dot{\Omega}_{ij}$ is the vorticity tensor. The principal components of the strain rate tensor $\dot{\varepsilon}_{1,2}$, which correspond to the maximum and minimum divergence, are given by equation 2.8. The strain invariants are given by the equation 2.9. The physical meaning of the first invariant $\dot{\varepsilon}_I$ is the mean divergence and $\dot{\varepsilon}_{II}$ corresponds to

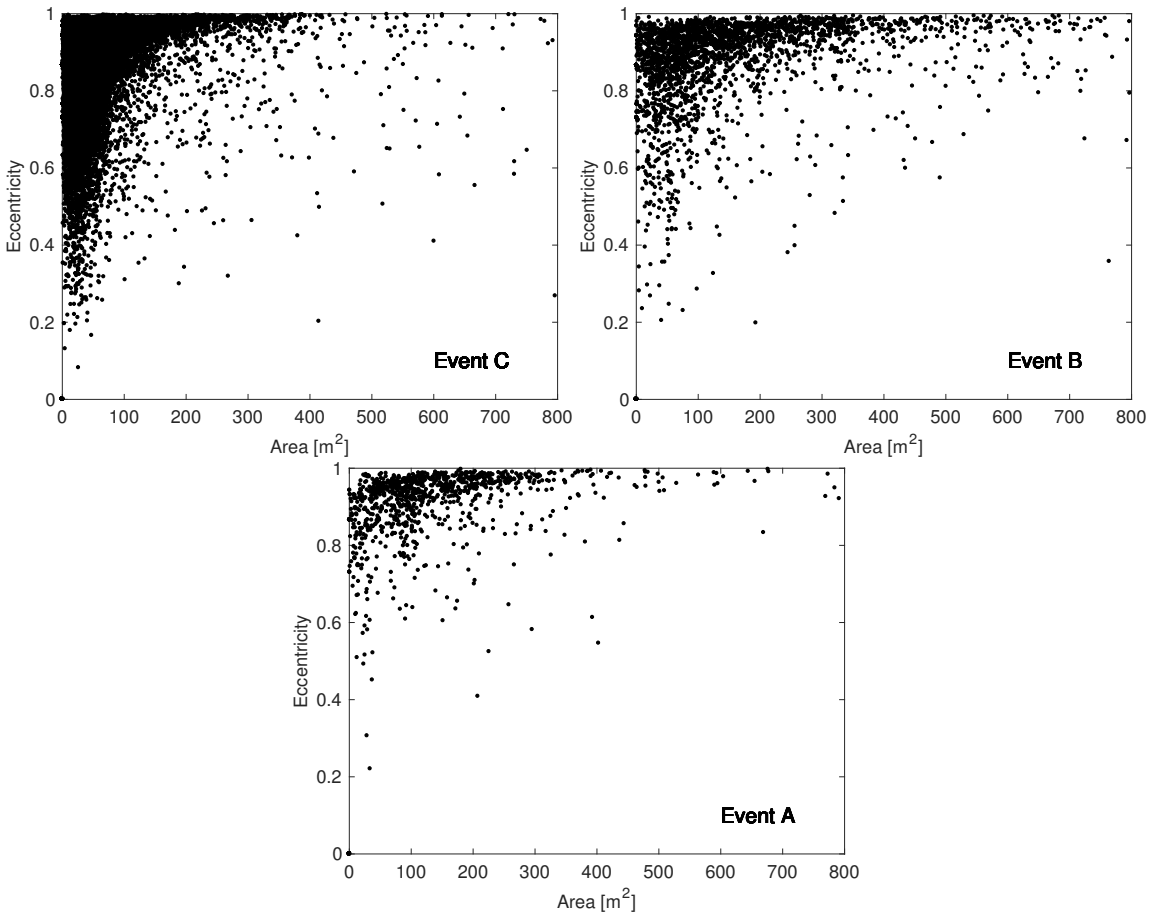

Figure 27: Eccentricity as a function of floe area for all images combine of all three events. The eccentricity is defined as the ratio of the distance between the foci and the major axis length. An eccentricity of 0 is a perfect circle and an eccentricity of 1 is a line. Although several floes have an eccentricity near 1 (some have an eccentricity of 0.995), none has a value of 1. Small floes have a larger range of eccentricity than large floes, which are more elongated. The number of floes, thus the number of data points, is different for each event

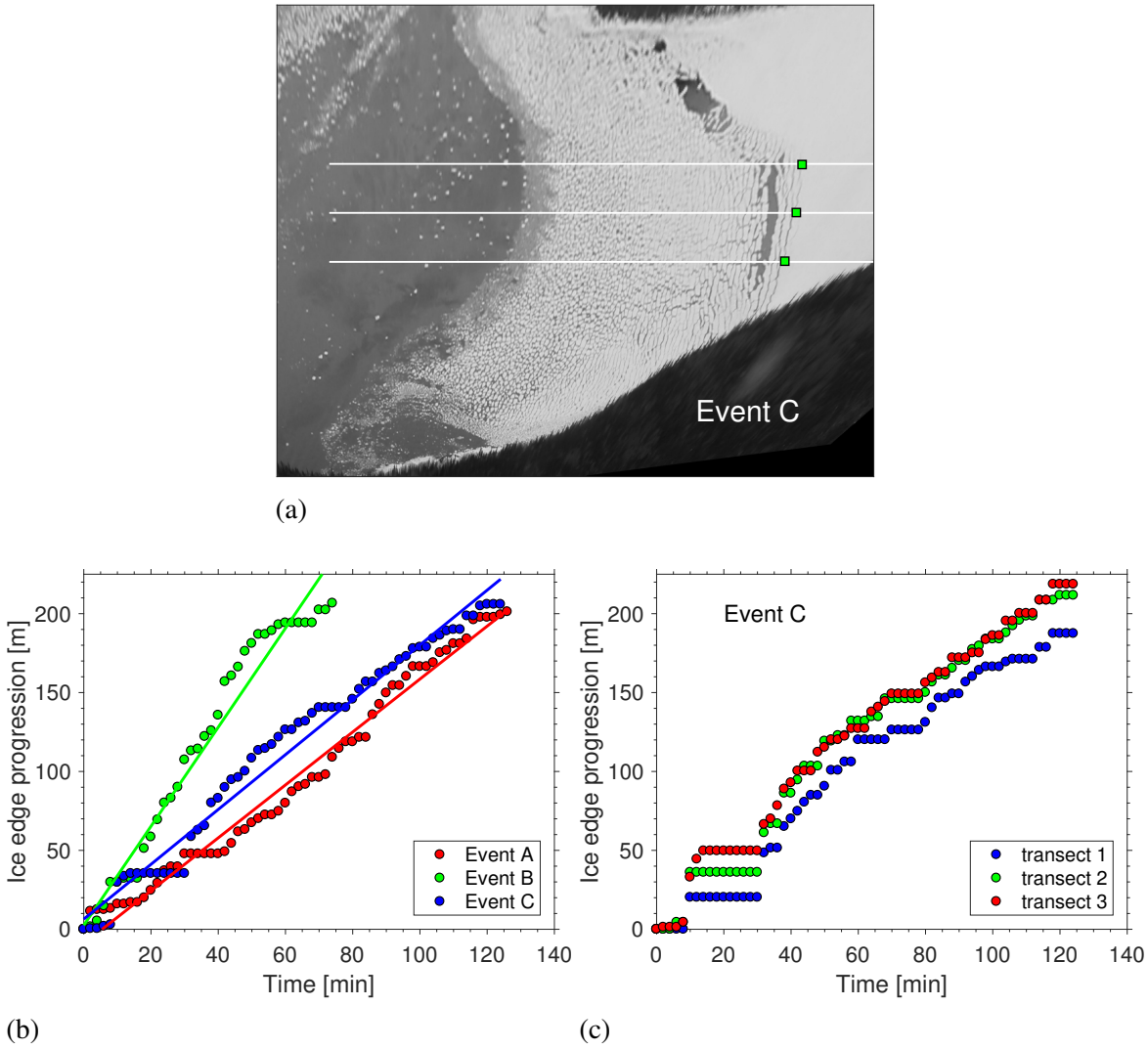

Figure 28: a) Position of the ice edge visually identified along three transects (green squares) for event C 8h30. b) Position of the ice edge averaged over the three transects for each event as a function of time. Lines correspond to a linear progression at the average speed. c) Progression of the ice edge for event C along the three transects.

the maximum shear strain. A quantity proportional to the kinetic energy $KE \propto \frac{v^2+u^2}{2}$ is also computed.

$$\dot{\varepsilon}_{1,2} = \frac{1}{2}(\dot{\varepsilon}_{11} + \dot{\varepsilon}_{22}) \pm \frac{1}{2}\sqrt{(\dot{\varepsilon}_{11}^2 - \dot{\varepsilon}_{22}^2) + 4\dot{\varepsilon}_{12}^2} \tag{2.8}$$

$$\dot{\varepsilon}_{\mathrm{I,II}} = \frac{1}{2}(\dot{\varepsilon}_1 \pm \dot{\varepsilon}_2) \tag{2.9}$$

The divergence field shows an interesting behavior (Figure 30). Bands of divergence (0.03 s^{-1}) and convergence (-0.015 s^{-1}) are present along the pack ice. Those bands represent the tendency of the floes to quickly get away from the ice pack once the first signs of break-up are visible.

In order to understand the linkage between floe size and the rheology, even though we do not know quantitatively the stresses acting on the floes, the deformation fields can be put in relation with ice concentration and the floe size. In order to do that, it is useful to create a grid, which has the same dimension as the deformation fields. Figure 31a is an example of the concentration of ice for one particular image. For each cell of the grid, the ratio of white pixels over black pixels is computed. Figure 22 shows that the floe size distribution changes over time during the break up event, but how can it be correlated with the deformation fields? To do so, we use the biggest floes of each cell of the deformation grid, called $D_{\max}$. Figure 32 shows two examples of deformation ($\dot{\varepsilon}_I$ and $\dot{\varepsilon}_{II}$) that reveal a correlation with the ice concentration and $D_{\max}$. Five images taken in the middle of event C are used in this figure to have a stronger statistical basis. Every point corresponds to a cell (40×40 pixels) in the deformation field that is compared to the same cell in the concentration and/or $D_{\max}$ field. Those results show quantitatively the intuitive notion that the magnitude of deformation increases when the floes are smaller and distant from each other.

In order to compare those results with other studies, it is useful to look at the different timescales characterizing the three events. Those timescales, which span orders of magnitude,

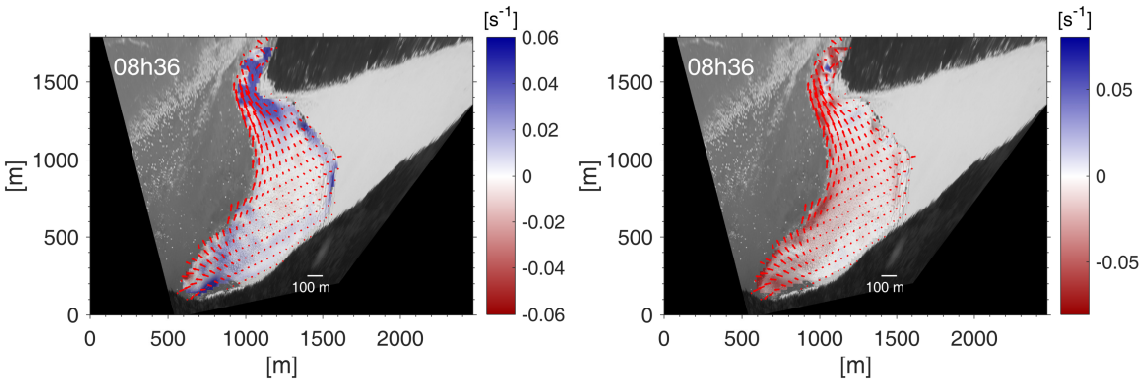

(a) $\dot{\varepsilon}_1$ (b) $\dot{\varepsilon}_2$

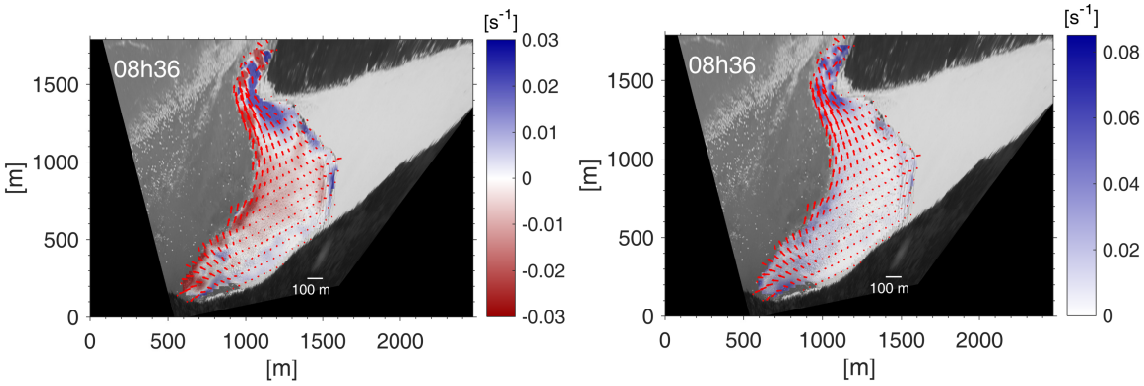

(c) Strain invariant $\dot{\varepsilon}_{\mathrm{I}}$ (d) Strain invariant $\dot{\varepsilon}_{\mathrm{II}}$

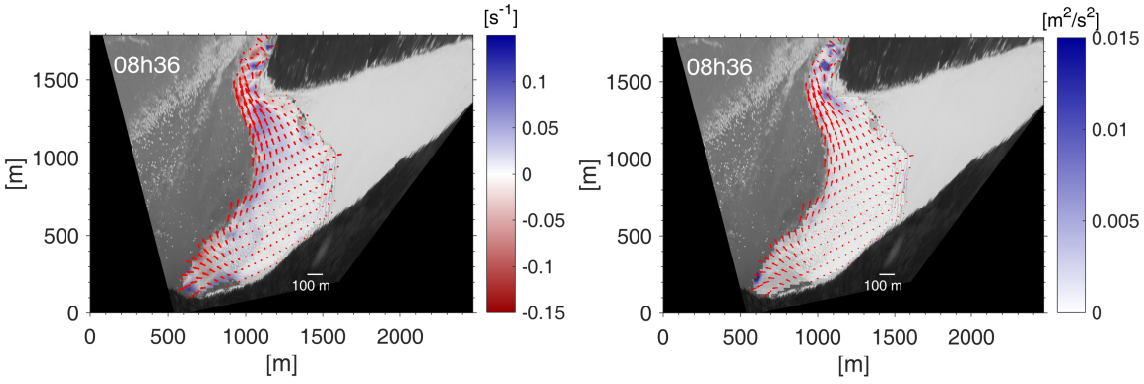

(e) Vorticity (f) Kinetic energy

Figure 29: Deformation field for one specific image taken at 8h36 during event C. Erratic behavior near the northem coast of the bay are considered aberrations. This behavior is particularly clear in panel c), in the northern part of the images as discussed above in section 2.2.

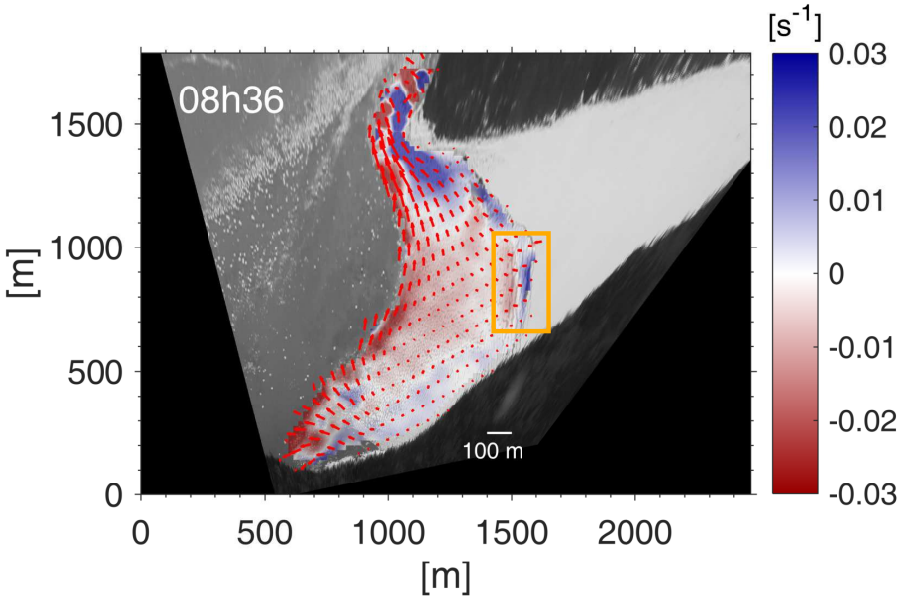

Figure 30: Zoom on the mean divergence $\dot{\varepsilon}_{\mathrm{I}}$ presented in Figure. 29. Band of divergence and convergence near the edge of the landfast ice are visible in the orange rectangle.

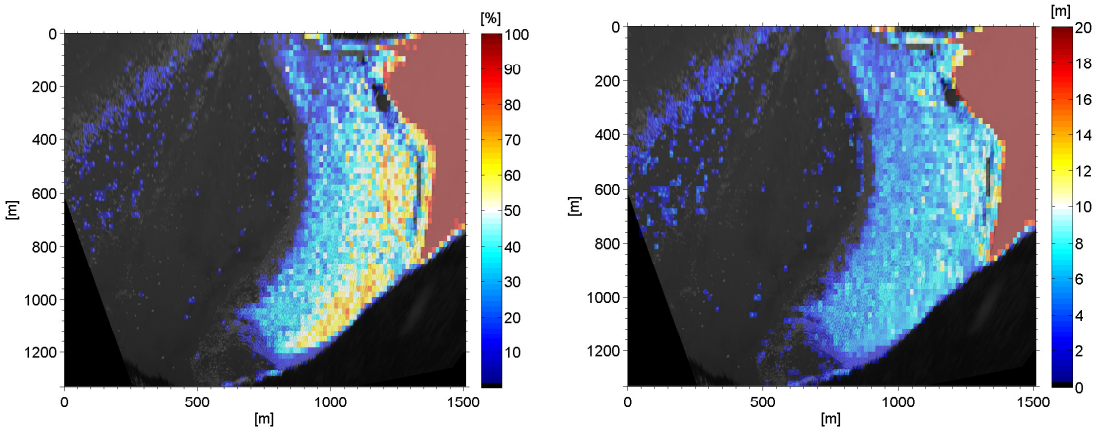

Figure 31: Concentration (left) and D_{max} (right) for event C 8h30EST.

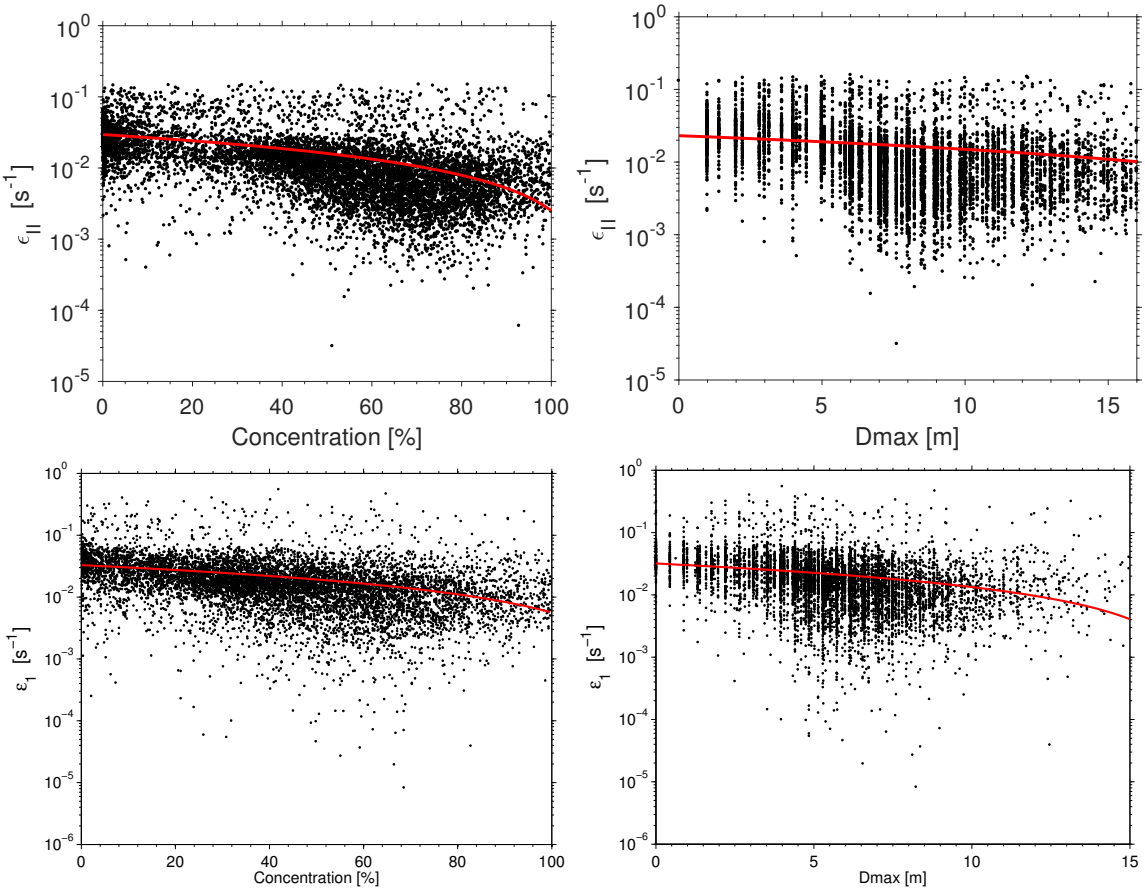

Figure 32: Example of two deformation fields ($\dot{\varepsilon}_I$ and $\dot{\varepsilon}_{II}$) correlated with concentration and $D_{\max}$. This graph shows that when the concentration increases or when the floes are larger, deformations are weaker. Since $D_{\max}$ is a multiple of a pixel length, the possible values are discrete, that is why vertical lines can be observed on the $D_{\max}$ graphs. The red line correspond to a linear fit based the minimization of the root-mean-square deviation.

Table 4: Different time scales that characterize the events. U is the average floe speed in the MIZ, L is the width of the bay (total distance travelled by floes before they leave the bay). All duration correspond to order of magnitude for the three events, except for the waves, where only 2016's event informations are available.

Time scale	**Symbol**	**Event A**	**Event B**	**Event C**
Event duration	T_{event}	2 h	2 h	2 h
Advection time scale	$T_{\text{adv}} = L/U$	1 h	1 h	2 h
Fragmentation time scale reshape process	T_{frac}	1 h	1 h	1 h
Deformation time scale length	T_{ϵ}	< 2 min	< 2 min	< 2 min
Waves	T_p	-	-	4 s

are summarized in Table 4. T_{event} is the event duration, T_{adv} corresponds to the time needed for floes to cross the entire bay from south to north and is related to a velocity scale U (mean drift speed) and a length scale L (width of the bay). T_{frac} is the time for the majority of the floes present in the mask to reach a stable size. T_{ϵ} is the timescale to see a notable deformation of the MIZ. Note that the pictures are taken every two minutes and deformation are notable from picture to picture for every event. Thus T_{ϵ} is less than two minutes, which is also supported by taking the inverse of typical strain rate values. Finally, T_p is the period of the waves. Even though we only have spectral wave data for event C, we can estimate the period from the waves visible on the picture.

2.4 Discussion

In this section, we attempt to link the waves, the formation of the MIZ and its evolution based on results from three ice break-up events in the baie du Ha! Ha!. First, we assume that in all three events waves are causing ice break-up through critical flexural failure. During a fragmentation event, in perfect conditions with a mono-chromatic wave travelling perpendicular to the edge of an ice plate, the failure is likely to appear at maximal stresses induced by the bending-gravity waves, which form lines of maximal stresses parallel to the plate edge. We would than expect very long ice bands with a constant width. In reality, cracking occurs so that instead of a very long band, anisotropic and elongated floes are obtained with their minor axis in the direction of the wave propagation and their major axis in the direction in which they are less bent by the waves. The orientation of the cracks in the ice pack is one clue that the surface waves visible during the event are the main source of fragmentation. Ice breaks up first along the failure lines that are somewhat parallel to the incident wave phase front and to the corresponding flexural wave in the ice (see Table 2). For events B and C (there is no wave information for event A) θ_{minor}, which is defined as is perpendicular to the cracks in the landfast ice cover, is almost parallel to the incident wave phase front with a deviation of 2% for event B and 8% for event C. The fact that failure lines are not perfectly parallel can be due to many factors (polychromatic wave spectrum, wave scattering, non-uniform wave packets, non-uniform ice plate, etc.). Another visual observation from the images that supports the assumption made in this paper that waves are responsible for ice fragmentation in the MIZ is presented in Figure 18. During event B, while surface waves are present in the bay, the rod-shaped floes that just separated from the landfast ice continue to break while they are carried by the current. When waves are no longer present in the bay, those floes preserve their shape.

The fragmentation process could have started before any crack was seen from the camera. In fact, the only event with available pre-event wave information (event C) shows that the time when waves were the strongest happens 12 hours before the separation of floes in captured by the camera. It is thus probable that the ice pack was partially broken up several

hours before tidal currents carried the floes away. During the 24 hours before the observation of event C by the camera, the modal wavelength λ_p is 25 ± 5 m and $\tilde{D}_{\text{ice}} = 11.6 \pm 1.7$ m. Since no wave information is available for event A, no comparison with $\tilde{D}_{\text{ice}}$ can be made. During event B, two wave fields with different wavelengths and orientations were captured by the camera, but the one with the largest modal wavelength is considered to be the major agent of fragmentation (see section 2.3.2). The modal wavelength during event B is therefore 24 ± 5 m and D_{ice} is 8.5 ± 1.3 m. No wave information prior to this particular event is available, which makes it hard to tell if the ice pack was already broken or not. The approximation made in some models (Dumont et al., 2011) that $D_{\text{ice}} = \lambda_p/2$ has a percentage deviation from $\tilde{D}_{\text{ice}}$ of 7 % for event B and 30 % for event C. Further events and analysis are needed to accentuate the link between D_{ice} and λ_p, and to increase statistical confidence. In our case, $D_{\text{ice}} = \lambda_p/2$ is more of an order of magnitude than an approximation. Mellor (1983) computed the distance x_* at which a semi-infinite ice plate bended will tend to break according to the Euler-Bernoulli theory. Assuming a thickness h of 0.6 ± 0.2 m, $E = 5.5$ GPa (Williams et al., 2013b), $\rho g = 10$ kN/m^3 and $\nu = 0.3$, equation 2.1 yields x_* ranging between 8.4 m and 14.1 m, which includes D_{ice} of all three events. Even though the range is wide, this equation gives an order of magnitude of x_* when no wave information is available.

One advantage of long time series is the possibility to follow the progression of the ice edge. Figure 28 shows an interesting behavior: an alternation between phases of important progression of the ice edge (which will be called "break-up phase") and phases where the ice edge does not change for several minutes (called "pause phase"). Such behavior indicates that once a group of floes is broken and detached from the ice pack, it takes a certain time before another "break-up phase" happens. Even if the ice plate is cracked by previous waves, this pause phenomena is observed. As an order of magnitude, for event C, the average pause phase duration is around five minutes and the period of the waves is $T = 4$ s, which gives an average of 75 wave impacts on the ice pack before another batch of floes is detached. This is an average, but since the averaged progression of the ice edge seems somewhat linear, as Figure 28b shows, this number could be interesting to compare in future events. An important

behavior shown in the Figure 28 is that the longer the breaking phase (a lot of floes got carried away in a short time), the longer the pause phase will lasts. This could be due to multiple phenomena. First, the pause phase can be associated with the time needed for groups of waves of sufficient amplitude to come and break the ice cover. Also, since the floes attenuate the waves, it is necessary to wait until they have left or until their size has decreased (the smaller their size, the lower their attenuation of the waves (Perrie and Hu, 1996)) for an other break-up phase to happen. This is consistent with the fact that the greater the break-up of the pack ice, the longer the time interval before another "break-up phase" occurs. Another possibility involves the phenomenon of fatigue. It is possible that once a group of floes cleared from the ice edge, a certain amount of time, associated with the fatigue of the ice cover, is necessary so that the flexural strength can be matched by the wave-induced stress. More work would be necessary in order to clearly distinguish what causes these "break-up / pause" phases.

As discussed above, it is possible that break-up events had already happened for a certain portion of the ice cover before they were seen by the camera. But the analysis of the floe size after the detachment from the ice pack shows that they keep breaking up over time. Figure 22 shows a clear evolution of the floe size for all three events. In order to describe this reshape process of the floes, it is useful to compare the floes when they leave the ice pack and once they reach an equilibrium state. The size of the most important group of floes at the equilibrium state $\tilde{D}_{\text{stable}}$ is smaller than $\tilde{D}_{\text{ice}}$ (see Table 3) by a few meters. What is not said by looking only at the $\tilde{D}_{\text{stable}}$ and $\tilde{D}_{\text{ice}}$, but visually apparent, is the isotropisation of the floes during that process. What is visually observed is that floes have elongated shapes shortly after the break-up and before they move away from the landfast ice cover. That unstable shape does not survive long under the effect of the waves, which leads to a more isotropic shape. In order to verify this observation more quantitatively, two sources of information need to be combined: the evolution of eccentricity and the evolution of the floe size. The measures of eccentricity are shown in Figure 24. At first, those results seem somewhat different from the visual observations since the eccentricity increases and decreases with about the same value at the start and the end on the event. That is because at the beginning there are very few

floes present in the masks. The increase of eccentricity corresponds to the phase were big elongated floes detached from the ice pack. The decrease in eccentricity corresponds to the reshape phase where floes drift and continue to break along the way. At the end of the event, the biggest floes are similar to the smallest in terms of eccentricity. This is because there is no longer a significant size difference between these two groups of floes. The evolution of ϕ (see Figure 22) corroborates this interpretation as the slope of the distribution is more pronounced at the equilibrium state than at the beginning of the event.

The analysis of perimeter and number of floes over time for event C and the visual observation of the data suggest a change of regimes after all the ice pack contained in the mask of event C is broken (even though there is not enough data to draw a clear conclusion). The first regime corresponds to a rapid increase of the number of floes and perimeter caused by the initial break-up from the ice pack. The second regime, smoother for both parameters, could correspond to the reshape process of the floes. In the second phase, the total perimeter and number of floes continue to increase, but the reshape process seems to be significantly slower.

One clear observation from the picture is that once floes have been detached from the ice pack, the dynamics change drastically. Event B is a good example where two different behaviors are observed, the plastic deformation of the ice plate, and the MIZ deformation. First, wind and current generate stresses on the ice cover via skin friction. Those stresses can generate a plastic deformation of the ice plate and can lead to ridging (compression stresses) or to the creation of leads through the ice (tension or shear stresses). Since the skin friction is proportional to the ice contact surface, those stresses need large spatial scales to develop. This is a well-observed behavior in the Arctic. At a much smaller scale, the presence of a lead in the northern part of Figure 18 (event B) can be attributed to this plastic behavior since it is to far from the ice edge to result from a flexural-wave fragmentation. This plastic behavior is different from the dynamics of the MIZ that have been studied above (see Figure 29). In the ice pack, deformations at large scale occurs along the leads, but the fragmentation of the

ice pack into floes ease the ice flow at a much smaller scale. For example, when a group of floes detaches from the ice edge, a band of divergence can been seen (see Figure 30). A few meters from the ice edge, a convergence band is also visible where the recently broken floes (which tend to take more space apart from each other) hit floes of the MIZ. More generally, once floes separate from the landfast ice, they begin to drift away from each other. This is a good example of a major dynamics change caused by the wave-induced fragmentation : 1) the slow, plastic and large scale deformation of the landfast ice cover induced by wind, current and tidal stresses and 2) the faster and fluid deformation of the MIZ. As discussed in the introduction, the dynamics in the MIZ is generally assumed to be dependant on the floe size and the ice concentration. That assertion is strengthened by the Figure 32 where the maximum shear strain ε_{II} and the principal component ε_1 are much smaller (by a factor of 4.5 and 5.75 respectively) where the ice concentration is maximum than where it is minimum. The same trend is observed for the graph in function of D_{max}. Many other parameters than the D_{max} and the ice concentration might be driving the MIZ dynamics observed during the events. The most important is the current. It is when the current is towards the bay that floes begin to be flushed during event C and around 12h00, when the tidal current changes its orientation, some of the floes comes back into the bay.

Typical timescales can be extracted from the temporal data and are in Table 4. The ratio L/U corresponded to the time needed for floes to cross the entire bay (south to north). For events A and B, the fragmentation process is not even finished when the first broken floes are already leaving the bay. This could be an important difference with the Arctic ice pack or other natural environments. Those timescales (see Table 4) are important to be able to compare the present results with further analysis.

2.5 Conclusion

The main objective of this paper was to characterize the evolution of the floe size distribution during wave-induced ice break-up events, a phenomenon that defines marginal ice zones. Using image processing tools, three ice fracture events were captured in baie du Ha! Ha! (Bic National Park, Rimouski, Canada) and analyzed. Algorithms made it possible to extract data on the morphology of the floes (area, perimeter, eccentricity, equivalent diameter), the progression of the ice edge and deformation fields of the MIZ in relation with wave condition assessed from various methods. The main conclusions of this work are:

1. Waves are the main agent of fragmentation of the landfast ice in the baie du Ha! Ha!
2. This fragmentation process is discontinuous (alternation between breaking and pause phases), but globally the ice edge progression into the landfast ice is somewhat linear.
3. The geometric characteristics of the floes resulting from the fragmentation of the sea ice depends on the wave conditions.
4. Past flexural stresses on the ice must be considered in order to properly characterize a break-up event of the pack.
5. The newly fragmented floes continue to evolve under the action of the waves until an equilibrium size is reached, which is accompanied by isotropisation of the floes.
6. Despite the isotropisation process of floes by the waves, the circular shape used in some models does not match what is observed in the baie du Ha! Ha! (even at equilibrium, floes have an eccentricity greater than 0.8).
7. Ice cover deformation highlights the existence of a rheological distinction between the broken-up marginal zone and the pack ice. This analysis also makes it possible to observe a divergence of the floes during the initial detachment of the pack ice.
8. The magnitude of deformation rates in the MIZ is correlated with floe size and concentration.

CONCLUSION GÉNÉRALE

L'un des objectifs de ce projet était de développer des outils de traitement d'images afin de mieux comprendre les interactions vagues-glace ainsi que l'évolution temporelle de la MIZ. Ces outils, ainsi que les données brutes, sont archivés, documentés et rendus disponibles via le dépôt Git https://gitlasso.uqar.ca/dumoda01/recon. Plusieurs améliorations pourraient être apportées aux algorithmes de traitement d'images. En effet, leur automatisation n'est pas complète et ces outils pourraient inclure des algorithmes plus évolués, tel que le *GVF snake* évoqué en introduction, ce qui limiterait la perte de glace lors des analyses et permettrait de mieux définir les propriétés géométriques des floes. Néanmoins, à partir de ces outils, nous avons pu analyser à peu de frais trois événements de fragmentation de la banquise par les vagues dans la Baie du Ha ! Ha !. Ces analyses ont notamment permis d'extraire pour la première fois l'évolution dans le temps de la géométrie des floes (aire, périmètre, excentricité, diamètre équivalent), la fragmentation de la banquise, ainsi que des champs de déformations de la MIZ. Le caractère original de ce projet vient de l'observation de l'évolution temporelle de ces différentes grandeurs en milieu naturel.

La Baie du Ha ! Ha ! a pour avantage d'être un site d'observation de la glace de mer facile d'accès. Plusieurs informations intéressantes sur la glace pourront y être mesurées dans de futurs travaux. Par exemple, il serait pertinent de mesurer plus précisément la distribution spatiale d'épaisseur ainsi que le module d'Young de la glace présente dans la baie afin de faciliter la caractérisation des événements de fragmentation qui s'y déroulent. Plus encore, il est possible d'y mesurer directement le coefficient d'atténuation des vagues par les floes et de caractériser la propagation d'ondes de fléchissement dans le couvert de glace. Toutes ces possibilités font de ce site d'étude un lieu privilégié pour l'étude de la zone marginale.

ANNEXE I

Mellor (1983) derives an expression for the distance x_* from the edge at which a thin elastic plate will break due to bending. After Hetényi (1971) , the bending moment M induced by a pressure P at the edge of semi-infinite plate extending in the positive x-axis direction is

$$M = -\frac{P}{\lambda} e^{-\lambda x} \sin \lambda x \tag{2.10}$$

where

$$\lambda = -\left(\frac{\rho g}{4EI}\right)^{\frac{1}{4}} \tag{2.11}$$

is the inverse of a flexural length scale that depends on the material density ρ, the gravitational acceleration g, Young's modulus E and the moment of inertia I of a rectangle plate of thickness h per unit length, given by

$$I = \frac{h^3}{12(1-\nu^2)}, \tag{2.12}$$

ν being the Poisson's ratio taking into account the orthogonal deformation of the material under stress. To find the distance from the edge located at $x = 0$ at which the bending moment is maximum, we differentiate with respect to x to obtain

$$\frac{\partial M}{\partial x} = P e^{-\lambda x} \left(\sin \lambda x - \cos \lambda x\right). \tag{2.13}$$

This expression is equal to zero whenever $\sin \lambda x = \cos \lambda x$, which is satisfied for $\lambda x = \pi/4$, and not $\lambda x = \pi/2$ as in Mellor (1983), and yields

$$x_* = \frac{\pi}{4}\left(\frac{Eh^3}{3\rho g(1-\nu^2)}\right)^{\frac{1}{4}}. \tag{2.14}$$

RÉFÉRENCES

Adrian, R. J., 2005. Twenty years of particle image velocimetry. In: Experiments in Fluids. Vol. 39. pp. 159–169.

Banfield, J. D., Raftery, A. E., 1992. Ice floe identification in satellite images using mathematical morphology and clustering about principal curves. J. Am. Stat. Ass. 87 (417), 7–16.

Blunt, J. D., Garas, V. Y., Matskevitch, D. G., Hamilton, J. M., 2012. Image Analysis Techniques for High Arctic, Deepwater Operation Support. In: OTC Arctic Technology Conference.

Bourgault, D., 2008. Shore-based photogrammetry of river ice. Can. J. Civ. Eng. 35 (1), 80–86.

Comiso, J. C., 2012. Large decadal decline of the arctic multiyear ice cover. J. Clim. 25 (4), 1176–1193.

Dumont, D., Kohout, A., Bertino, L., 2011. A wave-based model for the marginal ice zone including a floe breaking parameterization. J. Geophys. Res. 116, C04001.

Feltham, D. L., 2005. Granular flow in the marginal ice zone. Phil. Trans. Ser. A 363 (1832), 1677–1700.

Galbraith, P., Plourde, S., Starr, M., 2014. Suivi de l'état du Saint-Laurent : Les processus océanographiques dans l'estuaire et le golfe. Publication du Plan d'Action Saint-Laurent.

Herman, A., 2010. Sea-ice floe-size distribution in the context of spontaneous scaling emergence in stochastic systems. Phys. Rev. E 81 (6).

Herman, A., 2011. Molecular-dynamics simulation of clustering processes in sea-ice floes. Phys. Rev. E 84 (5).

Hetényi, M., 1971. Beams on elastic foundation: theory with applications in the fields of civil and mechanical engineering. University of Michigan.

Hibler III, W. D., 1979. A Dynamic Thermodynamic Sea Ice Model. J. Phys. Oceanogr. 9 (4), 815–846.

Holt, B., Martin, S., 2001. The effect of a storm on the 1992 summer sea ice cover of the Beaufort, Chukchi, and East Siberian Seas. J. Geophys. Res. 106 (C1), 1017–1032.

Horvat, C., Tziperman, E., 2015. A prognostic model of the sea-ice floe size and thickness distribution. Cryosphere 9 (6), 2119–2134.

Horvat, C., Tziperman, E., 2017. The evolution of scaling laws in the sea ice floe size distribution. J. Geophys. Res. 122 (9), 7630–7650.

Horvat, C., Tziperman, E., Campin, J. M., 2016. Interaction of sea ice floe size, ocean eddies, and sea ice melting. Geophys. Res. Lett. 43 (15), 8083–8090.

Kerr, A. D., Palmer, W. T., 1972. The deformations and stresses in floating ice plates. Acta Mech. 15 (1-2), 57–72.

Kohout, A. L., Williams, M. J. M., Dean, S. M., Meylan, M. H., 2014. Storm-induced sea-ice breakup and the implications for ice extent. Nature 509 (7502), 604–607.

Laikhtman, D., 1958. The drift of ice fields. Russian, Tr. Leningrad Gidrometeorol. Inst 7.

Langhorne, P. J., Squire, V. A., Fox, C., Haskell, T. G., 1998. Break-up of sea ice by ocean waves. Ann. Glaciol. 27, 438–442.

Lytle, V., Massom, R., Worby, A., Allison, I., 1997. Floe sizes in the east Antarctic sea ice zone estimated using combined sar and field data. Proceedings of the 3rd ERS Symposium on Space at the service of our Environment (1), 17–21.

Macqueen, J., 1967. Some methods for classification and analysis of multivariate observations. Proc. Fifth Berkeley Symposium on Mathematical Statistics and Probability 1 (233), 281–297.

Mellor, M., 1983. Mechanical behavior of sea ice. Tech. Rep. A131852, Cold Reg. Res. Eng. Lab.

Mellor, M., 1986. Mechanical behavior of sea ice. In: The geophysics of sea ice. Springer, pp. 165–281.

Meylan, M., Squire, V. A., 1994. The response of ice floes to ocean waves. J. Geophys. Res. 99, 891–900.

Paget, M. J., Worby, A. P., Michael, K. J., 2001. Determining the floe-size distribution of East Antartic sea ice from digital aerial photographs. Ann. Glaciol. 33, 94–100.

Pawlowicz, R., 2003. Quantitative visualization of geophysical flows using low-cost oblique digital time-lapse imaging. IEEE J. Ocean. Eng. 28 (4), 699–710.

Perovich, D. K., Jones, K. F., 2014. The seasonal evolution of sea ice floe size distribution. J. Geophys. Res. 119 (12), 8767–8777.

Perrie, W., Hu, Y., 1996. Air–Ice–Ocean Momentum Exchange. Part 1:Energy Transfer between Waves and Ice Floes. J. Phys. Oceanogr. 26 (9), 1705–1720.

Perrie, W., Hu, Y., 1997. Air-Ice-Ocean Momentum Exchange. Part II: Ice Drift. J. Phys. Oceanogr. 27, 1976–1996.

Petty, A. A., Feltham, D. L., Holland, P. R., 2013. Impact of Atmospheric Forcing on Antarctic Continental Shelf Water Masses. J. Phys. Oceanogr. 43 (5), 920–940.

Rabatel, M., Labbé, S., Weiss, J., 2015. Dynamics of an assembly of rigid ice floes. J. Geophys. Res. 120, 5887—-5909.

Reed, R. J., Campbell, W. J., 1960. Theory and observations of the drift of ice station alpha. Tech. rep., Washington University in Seattle.

Rothrock, D. A., Thorndike, S. A., 1984. Measuring the sea ice floe size distribution. J. Geophys. Res. 89, 6477–6486.

Ruzin, M., 1959. The wind drift of ice in a heterogeneous pressure field. Tr. Arkt. Antartkt. Inst.

Shen, H. H., Hibler, W. D., Leppäranta, M., 1986. On applying granular flow theory to a deforming broken ice field. Acta Mech. 63 (1-4), 143–160.

Shen, H. H., Hibler, W. D., Leppäranta, M., 1987. The role of floe collisions in sea ice rheology. J. Geophys. Res. (C7), 7085–7096.

Smith, D. a., Klinck, J. M., 2002. Water properties on the west Antarctic Peninsula continental shelf: a model study of effects of surface fluxes and sea ice. Deep-Sea Res. II 49 (21), 4863–4886.

Squire, V. A., 2007. Of ocean waves and sea-ice revisited. Cold Reg. Sci. Tech. 49 (2), 110–133.

Squire, V. A., Moore, S. C., 1980. Direct measurement of the attenuation of ocean waves by pack ice. Nature 283, 365–368.

Steele, M., 1992. Sea ice melting and floe geometry in a simple ice-ocean model. J. Geophys. Res. 97, 17729.

Steele, M., Morison, J. H., Untersteiner, N., 1989. The partition of air-ice-ocean momentum exchange as a function of ice concentration, roe size, and draft. J. Geophys. Res. 94 (C9), 12,739–12,750.

Steer, A., Worby, A., Heil, P., 2008. Observed changes in sea-ice floe size distribution during early summer in the western Weddell Sea. Deep-Sea Res. II 55 (8-9), 933–942.

Thielicke, W., Stamhuis, E. J., 2014. PIVlab - Time-Resolved Digital Particle Image Velocimetry Tool for MATLAB. J. Open Res. Soft. 2 (1), e30.

Thomson, J., Rogers, W. E., 2014. Swell and sea in the emerging Arctic Ocean. Geophys. Res. Lett. 41 (9), 3136–3140.

Toyota, T., Haas, C., Tamura, T., 2011. Size distribution and shape properties of relatively small sea-ice floes in the Antarctic marginal ice zone in late winter. Deep-Sea Res. II 58 (9-10), 1182–1193.

Toyota, T., Takatsuji, S., Nakayama, M., 2006. Characteristics of sea ice floe size distribution in the seasonal ice zone. Geophys. Res. Lett. 33 (2).

Williams, T. D., Bennetts, L. G., Squire, V. A., Dumont, D., Bertino, L., 2013a. Wave-ice interactions in the marginal ice zone. Part 1: Theoretical foundations. Ocean Model. 71, 81–91.

Williams, T. D., Bennetts, L. G., Squire, V. A., Dumont, D., Bertino, L., 2013b. Wave-ice interactions in the marginal ice zone. Part 2: Numerical implementation and sensitivity studies along 1D transects of the ocean surface. Ocean Model. 71, 92–101.

Xu, C., Prince, J. L., 1998. Snakes, shapes, and gradient vector flow. IEEE Transactions on Image Processing 7 (3), 359–369.

Zhang, J., Schweiger, A., Steele, M., Stern, H., 2015. Sea ice floe size distribution in the marginal ice zone: Theory and numerical experiments. J. Geophys. Res. 120, 3484–3498.

Zhang, Q., Skjetne, R., 2015. Image processing for identification of sea-ice floes and the floe size distributions. IEEE Trans. Geosci. Remote Sens. 53 (5), 2913–2924.

Zhang, Q., Skjetne, R., Su, B., 2013. Automatic image segmentation for boundary detection of apparently connected sea-ice floes. In: Port and Ocean Engineering under Arctic Conditions. pp. 27–38.